Blue-shifted ancyromonad channelrhodopsins for multiplex optogenetics

Elena G. Govorunova[1], Oleg A. Sineshchekov[1], Hai Li[1], Yueyang Gou[2,3], Hongmei Chen[2,3], Shuyuan Yang[4], Yumei Wang[1], Stephen Mitchell[5], Alyssa Palmateer[5], Leonid S. Brown[5], François St-Pierre[2,6,7,8], Mingshan Xue[2,3,9], and John L. Spudich[1*]

[1]Center for Membrane Biology, Department of Biochemistry & Molecular Biology, The University of Texas Health Science Center at Houston McGovern Medical School, Houston, TX 77030, USA

[2]Department of Neuroscience, Baylor College of Medicine; Houston, TX 77030, USA

[3]The Cain Foundation Laboratories, Jan and Dan Duncan Neurological Research Institute at Texas Children's Hospital; Houston, TX 77030, USA

[4]Department of Chemical and Biomolecular Engineering, Rice University, Houston, TX 77005, USA

[5]Department of Physics and Biophysics Interdepartmental Group, University of Guelph; Guelph, Ontario N1G 2W1, Canada

[6]Department of Biochemistry and Molecular Biology, Baylor College of Medicine, Houston, TX 77030, USA

[7]Systems, Synthetic, and Physical Biology Program, Rice University, Houston, TX 77005, USA

[8]Department of Electrical and Computer Engineering, Rice University, Houston, TX 7705, USA

[9]Department of Molecular and Human Genetics, Baylor College of Medicine, Houston, TX 77030, USA

[*]Correspondence: john.l.spudich@uth.tmc.edu (J.L.S.)

Abstract

Light-gated ion channels from protists (channelrhodopsins or ChRs) are optogenetic tools widely used for controlling neurons and cardiomyocytes. Multiplex optogenetic applications require spectrally separated molecules, which are difficult to engineer without disrupting channel function. Scanning numerous sequence databases, we identified three naturally blue-shifted ChRs from ancyromonads. They form a separate branch on the phylogenetic tree and contain residue motifs characteristic of anion ChRs (ACRs). However, only two conduct chloride, whereas the closely related *Nutomonas longa* homolog generates inward cation currents in mammalian cells under physiological conditions, significantly exceeding those by previously known tools with similar spectral maxima (peak absorption at ~440 nm). Measurements of transient absorption changes and pH titration of purified proteins combined with mutant analysis revealed the roles of the residues in the photoactive site. Ancyromonad ChRs could be activated by near-infrared two-photon illumination, a technique that enables the deeper-tissue optogenetic activation of specific neurons in three dimensions. Both ancyromonad ACRs allowed optogenetic silencing of mouse cortical neurons in brain slices. *Ancyromonas sigmoides* ACR (*Ans*ACR) expression in cholinergic neurons enabled photoinhibition of pharyngeal muscle contraction in live worms. Overall, our results deepen the mechanistic understanding of light-gated channel function and expand the optogenetic toolkit with potent, blue-shifted ChRs.

Impact statement: Ancyromonad channelrhodopsins advance our understanding of ionic selectivity and wavelength regulation in light-gated ion channels, and expand the toolkit for multiplexing with red-shifted fluorescent sensors.

Introduction

Channelrhodopsins (ChRs) are retinylidene proteins acting as photoreceptors that mediate photomotility in green flagellate algae (Sineshchekov, Jung et al. 2002) and are also found in other protist lineages. The chromophore is attached via a retinylidene Schiff base (RSB) linkage to a conserved lysine residue in the 7th transmembrane helix (TM7). Upon photoexcitation, ChRs generate passive ionic currents across the cell membrane and are used for optical control of excitable animal cells (optogenetics) (Deisseroth 2021, Piatkevich and Boyden 2023). The seven-transmembrane (7TM) domain is sufficient for channel activity; the role of the C-terminal domain, which comprises up to half of the polypeptide chain, remains unclear. A considerable diversity within the ChR family suggests a convergent evolution of light-gated channel function (Govorunova, Sineshchekov et al. 2022). ChRs form dimers (Volkov, Kovalev et al. 2017, Li, Huang et al. 2019) or trimers (Tucker, Sridharan et al. 2022, Morizumi, Kim et al. 2023), but their ionic conductance is intrinsic to individual protomers, unlike voltage- or ligand-gated channels, in which several protomers contribute to the channel pore. Anion channelrhodopsins (ACRs) generate photoinduced anion influx in mammalian cells; cation channelrhodopsins (CCRs) generate H^+ and Na^+ influx; and kalium channelrhodopsins (KCRs) generate K^+ efflux (Govorunova, Sineshchekov et al. 2022, Govorunova, Sineshchekov et al. 2023). ACRs and KCRs are used for optogenetic neuronal inhibition, and CCRs are used for neuronal activation.

Increasingly popular all-optical electrophysiology, i.e., simultaneous perturbation and measurement of membrane potential using light-sensitive actuators and reporters, respectively, in the same genetically defined cells (Hochbaum, Zhao et al. 2014) requires spectrally non-overlapping optogenetic tools. Even the most red-shifted ChRs retain sufficient sensitivity to blue light due to their relatively wide spectral bandwidth (Oda, Vierock et al. 2018, Govorunova, Sineshchekov et al. 2020). The development of red-light-absorbing genetically encoded fluorescent biosensors for monitoring neural activity (Sakamoto and Yokoyama 2025) opened up the possibility of pairing them with blue-shifted ChRs. Molecular engineering yielded several blue-shifted ChRs (Kato, Kamiya et al. 2015), but mutagenetic perturbations of the binding pocket frequently harm channel function. A complementary approach is exploring natural ChR diversity to search for molecules with desired biophysical properties optimized by evolution. Approximately ~1,000 ChR sequences are currently known, but a much smaller number has been functionally characterized (Govorunova, Sineshchekov et al. 2022).

Here, we identified and characterized three ChR variants from bacterivorous ancyromonad flagellates. Ancyromonads (also known as planomonads) represent a distinct major clade near the most commonly inferred root of the eukaryote tree (Brown, Heiss et al. 2018). We conducted automated and manual patch clamp analyses of photocurrents upon expression of ancyromonad ChR cDNAs in cultured mammalian cells under one- and two-photon excitation and monitored transient light absorption changes using detergent-purified proteins. We show that two ancyromonad ChRs are anion-selective, while the third and most blue-shifted ChR conducts metal cations. We expressed ancyromonad ACRs in mouse cortical pyramidal neurons and demonstrated photoinhibition of action potentials in acute brain slices. The nematode *Caenorhabditis elegans* is an attractive model for analyzing nervous system function by optogenetic manipulation (Bergs, Henss et al. 2022). We used this model organism to demonstrate that a

77 blue-shifted ancyromonad ACR enables efficient optogenetic inhibition of pharyngeal activity upon
78 expression in the cholinergic neurons.

79 **Results**

80 *Phylogeny, spectral sensitivity, and photon flux dependence*

81 Our bioinformatic search identified ChR homologs in the ancyromonads *Ancyromonas sigmoides,*
82 *Fabomonas tropica,* and *Nutomonas longa; Ancoracysta twista,* a predatory flagellate placed in the newly
83 established supergroup Provora (Tikhonenkov, Mikhailov et al. 2022); the diatom *Odontella aurita*; and
84 *Paraphysoderma sedebokerense*, a chytrid-like fungus from the phylum Blastocladiomycota. Phylogenetic
85 analysis placed the ancyromonad ChRs on a separate branch of the ACR tree together with their
86 metagenomic homologs from the TARA Oceans database (Figure 1A). The *A. twista* and *O. aurita* homologs
87 clustered with known stramenopile ACRs. The *P. sedebokerense* sequence showed only a distant homology
88 to previously known ACRs. Figure 1 – figure supplement 1 shows a protein alignment of their 7TM domains
89 compared with *Gt*ACR1, the best-characterized ACR from the cryptophyte *Guillardia theta* (Govorunova,
90 Sineshchekov et al. 2015, Li, Huang et al. 2019). All these sequences exhibit a non-carboxylate residue at
91 the primary counterion position, corresponding to Asp85 in TM3 of *Halobacterium salinarum*
92 bacteriorhodopsin (BR), marked by the red arrow in Figure 1 – figure supplement 1, as found in all known
93 ACRs. The 2nd carboxylate in the photoactive site, contributed by TM7 and corresponding to Asp212 of BR,
94 is replaced with Glu in the *N. longa* sequence, and with Gln in the *P. sedebokerense* sequence (the blue
95 arrow in Figure 1 – figure supplement 1).

96 We expressed cDNAs encoding the 7TM domains of seven homologs fused to a C-terminal mCherry tag in
97 human embryonic kidney (HEK293) cells and recorded photocurrents using manual patch clamping. All
98 three ancyromonad ChRs generated robust photocurrents and showed maximal sensitivity in the blue
99 spectral range (Figure 1B). Based on their ionic selectivities (see the next section), we named the *A.*
100 *sigmoides, F. tropica,* and *N. longa* homologs *Ans*ACR, *Ft*ACR, and *Nl*CCR, respectively. The spectral
101 sensitivity of the *A. twista* and *O. aurita* homologs was in the blue-green range (Figure 1 – figure
102 supplement 2, left). Partial replacement of Cl^- in the bath with non-permeable aspartate shifted reversal
103 potential (V_r) to more positive values, confirming their anion selectivity (Figure 1 – figure supplement 2,
104 middle and right). We named them *At*ACR, *Oa*ACR1, and *Oa*ACR2. However, their photocurrents were
105 smaller than those of the ancyromonad homologs or exhibited strong desensitization (reduction of
106 photocurrents during illumination), so we did not characterize them in more detail. No photocurrents were
107 detected in cells transfected with the *P. sedebokerense* homolog, although its expression and membrane
108 targeting were evident from the tag fluorescence. Therefore, we named this protein *Pars*R, where R means
109 "rhodopsin".

110 Next, we expressed the constructs encoding ancyromonad ChRs in *Pichia pastoris.* We purified the
111 proteins using a mild detergent yielding 0.25, 0.35, and 0.15 mg purified protein per L culture for *Ans*ACR,
112 *Ft*ACR, and *Nl*CCR, respectively. The absorption spectra of the purified proteins (Figure 1C) were slightly
113 blue-shifted from the respective photocurrent action spectra (Figure 1 – figure supplement 3), likely due
114 to the presence of non-electrogenic *cis*-retinal-bound forms. The presence of such forms, explaining the
115 discrepancy between the absorption and the action spectra, was verified by HPLC in KCRs (Tajima et al.
116 2023, Morizumi et al., 2025). To test the possibility of using *Ans*ACR in multiplex optogenetics, we co-
117 expressed it with the red-shifted CCR Chrimson (Klapoetke et al., 2014) fused to an EYFP tag in HEK293
118 cells. We measured the action spectrum of the net photocurrents with 4 mM Cl^- in the pipette, matching

the conditions in the neuronal cytoplasm (Doyon, Vinay et al. 2016). Figure 1D, black shows that the direction of photocurrents was hyperpolarizing upon illumination with λ<500 nm and depolarizing at longer wavelengths. A shoulder near 520 nm revealed a FRET contribution from EYFP (Govorunova, Sineshchekov et al. 2020), which was also observed upon expression of the Chrimson construct alone (Figure 1D, red). Figures 1E and F show the dependence of the peak photocurrent amplitude and reciprocal peak time, respectively, on the photon flux density for ancyromonad ChRs and *Gt*ACRs. The current amplitude saturated earlier than the time-to-peak for all tested ChRs. Figure 1 – figure supplement 4A-E shows normalized photocurrent traces recorded at different photon densities. Quantitation of desensitization at the end of 1-s illumination revealed a complex light dependence (Figure 1, Figure Supplement 4F). Figure 1 – figure supplement 5 shows normalized photocurrent traces recorded in response to a 5-s light pulse of the maximal available intensity and the magnitude of desensitization at its end.

Characterization of ancyromonad ChRs by automated patch clamping

We used the fully automated planar patch clamp platform SyncroPatch 384 to characterize ancyromonad ChRs' photocurrents. This instrument uses KF-based internal and NaCl-based external solutions to promote gigaseal formation (Supplementary File 1). Figure 2A-C shows photocurrent traces evoked by 200-ms light pulses. The SyncroPatch enables unbiased estimation of the photocurrent amplitude because the cells are drawn into the wells without considering their tag fluorescence, unlike manual patch clamp studies in which the experimenter selects the fluorescent cells. Figure 2 – figure supplement 1A, B shows that the mean *Ans*ACR photocurrent measured by the SyncroPatch was significantly larger than the mean *Ft*ACR photocurrent, and the mean *Nl*CCR photocurrent was significantly larger than that of *Platymonas subcordiformis* channelrhodopsin 2 (*Ps*ChR2), a previously known excitatory optogenetic tool with a similar blue-shifted spectrum (Govorunova, Sineshchekov et al. 2013, Chen, Duan et al. 2022).

The voltage dependencies of photocurrents (IV curves) are shown in Figure 2D-F. *Ans*ACR and *Ft*ACR showed similarly negative V_r values, suggesting higher relative permeability to Cl^- than F-, as earlier found in *Gt*ACRs by manual patch clamping (Govorunova, Sineshchekov et al. 2015). The V_r values of the peak current and that at the end of illumination were not significantly different by the two-tailed Wilcoxon signed-rank test (Fig. 2G), indicating no change in the relative permeability during illumination. Unexpectedly, the *Nl*CCR photocurrents reversed near 0 mV (Fig. 2F, G). One reason for this behavior could be equal permeabilities of this ChR to Cl^- and F^-. However, when Cl^- in the external solution was partially replaced with bulky, non-permeable aspartate, only *Ans*ACR and *Ft*ACR showed substantial V_r shifts to more positive values, which confirmed their permeability to Cl^-, but no such shift was detected in *Nl*CCR (Figure 2H-J, red symbols). Control experiments conducted by manual patch clamping with the Cl^--based pipette solution confirmed these observations (Figure 2 – figure supplement 2). Upon replacing Cl^- with NO_3^-, *Ans*ACR and *Ft*ACR, but not *Nl*CCR, showed V_r shifts to more negative values (Figure 2H-J, green), as did *Gt*ACRs examined by manual patch clamping (Govorunova, Sineshchekov et al. 2015), which indicated higher relative permeability to NO_3^- than to Cl^-. *Ft*ACR exhibited a larger V_r shift in NO_3^- than *Ans*ACR ($p = 2.6E10-5$ by the two-tailed Mann-Whitney test). Replacing Na^+ with N-methyl-D-gluconate ($NMDG^+$) resulted in a negative V_r shift in *Nl*CCR but not the other tested variants (Figure 2H-J, blue), suggesting that *Nl*CCR is permeable to Na^+. Figure 2 – figure supplement 1C, D compares *Nl*CCR with the typical cation-selective *C. reinhardtii* channelrhodopsin 2 (*Cr*ChR2), assessed using the same assay. Acidifying the external solution to pH 5.4 or replacing Na^+ with K^+ did not affect the V_r of any ancyromonad ChR (Figure

2, grey and violet). We conclude that only *Ans*ACR and *Ft*ACR are anion-selective, but *Nl*CCR conducts monovalent metal cations despite its sequence homology to the other two variants.

Channel gating and photochemical transitions under single-turnover conditions

Photocurrents evoked by continuous light pulses do not accurately reflect channel kinetics because different ChR molecules absorb photons at different times. Further complications result from photon absorption by photocycle intermediates. We conducted manual patch clamp recordings upon 6-ns laser flash excitation to analyze channel gating. *Ans*ACR and *Ft*ACR photocurrents exhibited biphasic rise and decay (Figure 3A, D), as the earlier characterized *Gt*ACR1 (Sineshchekov, Govorunova et al. 2015). The IV curves of all kinetic components revealed the same V_r values (Figure 3 – figure supplement 1A, B), meaning no ion selectivity changes occur during the single-turnover photocycle. Next, we analyzed transient absorption changes in detergent-purified *Ans*ACR and *Ft*ACR. In contrast to *Gt*ACR1, we could not find a clear indication of the accumulation of a blue-shifted L intermediate. After an initial (unresolved) decay of a K-like intermediate, red-shifted absorbance temporally increased in both ancyromonad ACRs, reaching a maximum at 100-200 µs (Figure 3B, E, red), i.e., in the time domain of fast channel opening. This red-shifted intermediate could be a long-lived K or an unusual red-shifted L. In *Ft*ACR, an additional slower increase in the red-shifted absorbance likely reflected the formation of an O-like intermediate (Fig. 3E, red). Accumulation of the M intermediate absorbing in the UV range was only 10 (*Ans*ACR) or 2 times (*Ft*ACR) slower than channel opening (Figure 3C, F), although in *Gt*ACR1 it was 50 times slower (Sineshchekov, Govorunova et al. 2015). Also, in contrast to prior observations in *Gt*ACR1, no temporal correlation was found between M formation and fast channel closing and between M decay and slow channel closing in ancyromonad ACRs. *Nl*CCR, the most blue-shifted among the ancyromonad ChRs we identified, has negligible absorption at 532 nm, the excitation laser's wavelength; therefore, its photochemical conversions could not be probed with our flash photolysis setup. In contrast to *Ans*ACR and *Ft*ACR, *Nl*CCR's laser-flash-induced photocurrent kinetics showed single exponential opening and closing in Cl^- and did not change upon its substitution with Asp^- in the bath solution (Figure 3 – figure supplement 1C,D).

While all ACRs have a non-carboxylate residue homologous to Asp85 in BR, the second counterion homologous to Asp212 in BR remains protonatable (Figure 1 – figure supplement 1, red arrow). To estimate the pK_a of this counterion, we performed pH-titration of the absorption spectra (Fig. 4A-C). The titration curves revealed two transitions in all ancyromonad ChRs. Acidification caused a transition to longer peak absorption wavelengths, as expected upon protonation of the counterion, with pK_{a1}s ~3.9, 2, and 3.4 for *Ans*ACR, *Ft*ACR, and *Nl*CCR, respectively. The maximum amplitude of this transition in *Ans*ACR (~8 nm) exactly corresponded to the 8-nm red shift of the photocurrent action spectrum in the *Ans*ACR_D226N mutant (Fig. 4D). The D226N mutation did not suppress photocurrent, but simplified its kinetics (Fig. 4E). Instead of the biphasic opening and closing observed in the WT, only two exponentials were sufficient to fit the D226N mutant's current, one for opening and one for closing. This observation suggested the role of Asp226 in channel gating, which was confirmed by analysis of the voltage dependence of the closing τ (Fig. 4F). Upon shifting to positive voltages, both components of channel closing accelerated in the WT, but the single-exponential closing slowed in the mutant, which suggests that oppositely directed charge movements control channel closing in the WT and the mutant.

Further acidification caused a transition to shorter wavelengths with similar pK_{a2}s in both purified ancyromonad ACRs and only a slightly lower pK_{a2} in *Nl*CCR (Fig. 4A-C). It most probably reflects binding Cl^-

203 in the photoactive site, as in archaeal rhodopsins (Shimono, Kitami et al. 2000). On the other hand, in
204 contrast to *Natronomonas pharaonis* halorhodopsin (Váró, Brown et al. 1996), no blue spectral shift was
205 detected in detergent-purified *Ans*ACR at neutral pH upon an increase in the Cl^- concentration (Figure 4 –
206 figure supplement 1), which argued against Cl^- binding in the RSB region under these conditions.

207 Mutagenetic introduction of Glu in *Ans*ACR in the position of the primary acceptor in BR (the G86E
208 mutation) led to the appearance of an additional spectral transition with pK_a 7.4 upon pH titration of
209 purified protein (Fig. 4G). An extremely fast M-like UV-absorbing intermediate absent in the WT was
210 observed in the mutant (Fig. 4H, red). Its rise and decay τ corresponded to the rise and decay τ of the fast
211 positive current recorded from *Ans*ACR_G86E at 0 mV and neutral pH, superimposed on the fast negative
212 current reflecting the chromophore isomerization (Figure 4I, upper black trace). We interpret this positive
213 current as an intramolecular proton transfer to the mutagenetically introduced primary acceptor (Glu86),
214 which was suppressed by negative voltage (Figure 4I, lower black trace). Acidification increased the
215 amplitude of the fast negative current ~10-fold (Figure 4I, black arrow) and shifted its V_r ~100 mV to more
216 depolarized values (Figure 4 – figure supplement 2A). This can be explained by passive inward movement
217 of the RSB proton along the large electrochemical gradient. Remarkably, the G86E mutation suppressed
218 channel current at neutral pH, but acidification of the bath to pH 5.4 recovered it (Figure 4I, red arrow).
219 The full current trace recorded under acidic conditions could be deconvoluted into four components with
220 τ 30 µs, 80 µs, 1.5 ms, and 640 ms, revealing that the mutation slowed channel closing 6-fold. Replacement
221 of Cl^- with Asp^- caused a ~40-mV shift of the channel current's V_r (Figure 4 – figure supplement 2B),
222 indicating that the mutant channel remained Cl^- selective. These results confirm that the absence of a
223 negative charge at the site corresponding to BR's primary acceptor is the ultimate condition for anion
224 channel function.

225 Strong alkalization caused simultaneous depletion of absorption in the visible range, the appearance of
226 the M-like states (at 368 nm in the wild-type *Ans*ACR and 355 nm in the *Ans*ACR_G86E mutant), and a
227 substantial absorption increase at 297 nm, reflecting deprotonation of the RSB and a strong perturbation
228 of the protein band (Figure 4 – figure supplement 2C). Analysis of the pH dependence of three parameters
229 (absorption depletion in the visible range, absorption rise in the M-like states' range, and absorption rise
230 at 297 nm) yielded similar pK_a values, which were 11.1 and 10.7 for the WT and G86E, respectively (Figure
231 4 – figure supplement 2D). These high pK_a values may explain the high photostability of this protein, as
232 hundreds of laser flashes did not cause its measurable bleaching.

233 The glutamate in the middle of TM2 corresponding to Glu68 of *Gt*ACR1 is conserved in most ACRs,
234 including *Ft*ACR, but is replaced with Gln in *Ans*ACR (Figure 1 – figure supplement 1, black arrow).
235 Introducing the Q48E mutation in *Ans*ACR accelerated channel closing and slowed channel opening,
236 making the photocurrent rise and decay monophasic (Figure 4 – figure supplement 3A,B).

237 *The retinal-binding pocket and color tuning*

238 The λ_{max} of rhodopsins is regulated by the retinal chromophore geometry and steric and electrostatic
239 interactions of the chromophore with amino acid residues of the retinal-binding pocket (Hoffmann, Wanko
240 et al. 2006, Karasuyama, Inoue et al. 2018). Surprisingly, *Nl*CCR, the most blue-shifted among
241 ancyromonad ChRs, features three residues typical of red-shifted microbial rhodopsins (Figure 5A). The
242 first is Phe at the primary counterion position (Asp85 in BR), also found in RubyACRs from Labyrinthulea,
243 the most red-shifted ChRs so far identified (Govorunova, Sineshchekov et al. 2020). The residues

homologous to BR's Met118 near the β-ionone ring and Ala215 preceding the RSB lysine in the polypeptide chain are responsible for red-shifted absorption in many microbial rhodopsins (Shimono, Iwamoto et al. 2000, Engqvist, McIsaac et al. 2015, Oda, Vierock et al. 2018, Oppermann, Rozenberg et al. 2024) but are conserved in all three blue-absorbing ancyromonad ChRs. In *Gt*ACR1 (λ_{max} 515 nm, (Govorunova, Sineshchekov et al. 2015, Sineshchekov, Li et al. 2016)), the only ACR with published atomic structures (Kim, Kato et al. 2018, Li, Huang et al. 2019), the corresponding residues are Ser97, Cys133, and Cys237 (Figure 5B). As expected, the S97F, C133M, and C237A mutations red-shifted the *Gt*ACR1 spectrum (Figure 5C). The opposite F104S, M143C, and A242C mutations at the corresponding sites in the RubyACR from *Hondaea fermentalgiana* (*Hf*ACR1) caused large blue spectral shifts (Figure 5D). However, the corresponding mutations F85S, M141C, and A236C red-shifted the *Nl*CCR spectrum (Figure 5E). The same paradoxical behavior was observed upon mutation of the Met118 homolog to Val, which blue-shifted the *Hf*ACR1 spectrum but red-shifted the ancyromonad ChR spectra (Figure 5F-H). Replacement of the Ala215 homolog with Cys or Ser did not change the *Ans*ACR and *Ft*ACR spectra (Figure 5 – figure supplement 1A, B).

In blue-shifted ChRs such as *Ps*ChR2 (Govorunova, Sineshchekov et al. 2013) and *Klebsormidium nitens* channelrhodopsin (*Kn*ChR) (Tashiro, Sushmita et al. 2021), the position of BR's Met118 is occupied by Gly or Ala (Figure 5A), which, together with the Ala four residues downstream (BR's Gly122), rotates the β-ionone ring out of the plane of the polyene chain, shrinking the *p*-conjugation and blue-shifting the spectrum (Wang, Natsume et al. 2025). The Ala corresponding to BR's Gly122 is also found in *Ans*ACR and *Nl*CCR (Figure 5A), but the *Ans*ACR_M134A/G and *Nl*CCR_M141A/G mutations did not change the spectra, nor did the *Ft*ACR_M140G_V144A mutation (Figure 5 – figure supplement 1A-C). These observations suggest that the residue geometry and/or interactions in the retinal-binding pocket in ancyromonad ChRs differ from the earlier studied microbial rhodopsins.

The residue position corresponding to BR's Leu93 is the color switch between blue- and green-absorbing proteorhodopsins (BPRs and GPRs, (Man, Wang et al. 2003)). *Ans*ACR exhibits a Gln residue in this position, as do BPRs, but *Ft*ACR has Leu, as do GPRs, and *Nl*CCR has Met (Figure 5A). The *Ft*ACR_L96Q and *Nl*CCR_M93Q mutations blue-shifted the spectra 20 and 7 nm, respectively (Figure 5I, J), indicating that this residue position contributes to color tuning in ancyromonad ACRs. *Nl*CCR, the most blue-shifted among ancyromonad ChRs, differs from *Ans*ACR and *Ft*ACR at the positions corresponding to Ser89 and Glu233 (*Nl*CCR numbering), and from *Ft*ACR, also at the position of Pro235 (the corresponding residues in *Gt*ACR1 are Thr101, Asp234, and Leu236, Figure 5A). The S89T, E233D, and P235I mutations red-shifted the *Nl*CCR spectrum (Figure 5K), indicating that these three positions contribute to the blue shift of wild-type *Nl*CCR compared with *Ans*ACR and *Ft*ACR. However, the T90S mutation did not change the *Ans*ACR spectrum, and the D226E mutation and a combination of the two mutations caused red spectral shifts in *Ans*ACR (Figure 5 – figure supplement 1D). Supplementary File 2 contains the λ values of the half-maximal amplitude of the long-wavelength slope of the spectrum, which can be estimated more accurately from the action spectra than the λ of the maximum.

Two-photon excitation

Optical manipulation of neuronal activity in dense tissue commonly relies on two-photon (2P) excitation, which is based on the nearly simultaneous absorption of two infrared photons, equivalent to the absorption of one photon in the visible range (Emiliani, Entcheva et al. 2022). To determine the 2P activation range of *Ans*ACR, *Ft*ACR, and *Nl*CCR, we conducted raster scanning using a conventional 2P laser,

286 varying the excitation wavelength between 800 and 1,080 nm (Figure 6 – figure supplement 1). All three
287 ChRs generated detectable photocurrents with action spectra showing maximal responses at ~925 nm for
288 *Ans*ACR, 945 nm for *Ft*ACR, and 890 nm for *Nl*CCR (Figure 6A). These wavelengths fall within the excitation
289 range of common Ti:Sapphire lasers, which are widely used in neuroscience laboratories and can be tuned
290 between ~700 nm and 1,020-1,300 nm. To assess desensitization, cells expressing *Ans*ACR, *Ft*ACR, or *Nl*CCR
291 were illuminated at the respective peak wavelength of each ChR at 15 mW for 5 seconds. *Gt*ACR1 and
292 *Gt*ACR2, previously used in 2P experiments (Forli, Vecchia et al. 2018, Mardinly, Oldenburg et al. 2018),
293 were included for comparison. The normalized photocurrent traces recorded under these conditions are
294 shown in Figure 6B-F. The absolute amplitudes of 2P photocurrents at the peak time and at the end of
295 illumination are shown in Figure 6G and H, respectively. All five tested variants exhibited comparable levels
296 of desensitization at the end of illumination (Figure 6I).

297 *Optogenetic inhibition of cortical neurons in mouse brain slices*

298 To test the silencing efficiencies of *Ans*ACR and *Ft*ACR in mouse brain slices, we selectively expressed their
299 7TM domains fused with EYFP in the layer 2/3 pyramidal neurons of the somatosensory cortex by *in utero*
300 electroporation at embryonic day 15. We prepared acute brain slices from 4-6-week-old mice and EYFP
301 fluorescence was observed in the layer 1, layer 2/3 and layer 5, indicating clear *Ans*ACR-EYFP and *Ft*ACR-
302 EYFP expression in dendrites, somata, and axons, respectively (Figure 7 – figure supplement 1A). We
303 performed whole-cell current clamp recordings from *Ans*ACR- or *Ft*ACR-expressing neurons (for solution
304 compositions, see Material and Methods). *Ans*ACR- and *Ft*ACR-expressing neurons showed the resting
305 membrane potential, input resistance, and capacitance (Figure 7 – figure supplement 1B) similar to the
306 typical values of untransfected cortical neurons (Xue, Atallah et al. 2014, Chen, Cai et al. 2020). When
307 positive currents were injected into the somata to excite neurons, photoactivation of *Ans*ACR and *Ft*ACR
308 suppressed the current-evoked action potentials, demonstrating the potency of these proteins as
309 optogenetic silencers of mouse cortical neurons (Figure 7). We also observed that at rest or when a small
310 negative current (e.g., -0.1 nA) was injected, the neurons could generate a single action potential at the
311 beginning of photostimulation (Figure 7A, B), possibly caused by axonal depolarization, as reported in
312 *Gt*ACR-expressing neurons (Mahn, Gibor et al. 2018, Messier, Chen et al. 2018).

313 Earlier studies have shown that photoactivation of *Gt*ACRs induces axonal depolarization and synaptic
314 transmission in some ACR^+ neurons owing to the high intracellular Cl^- concentration at the axons (Mahn,
315 Gibor et al. 2018, Messier, Chen et al. 2018). Indeed, when we recorded from ACR^- neurons in the
316 electroporated cortical region, we found that photoactivation of either *Ans*ACR- or *Ft*ACR-induced
317 excitatory post-synaptic currents (Figure 7 – figure supplement 1C, D), similar to other tested light-gated
318 Cl^- channels.

319 *Optogenetic inhibition of pharyngeal function in live C. elegans*

320 To test *Ans*ACR as an optogenetic inhibitory tool in the context of an intact behaving animal, we expressed
321 the encoding construct fused to a C-terminal EYFP tag in the *C. elegans* cholinergic neurons using the *unc-*
322 *17* promoter (a scheme of the expression construct is shown in Figure 8A). C. *elegans* feeds on bacteria by
323 rhythmic contractions and relaxations (pumping) of its pharynx. The cholinergic pharyngeal neurons,
324 primarily MC neurons, entrain the pharyngeal muscle rhythm (Trojanowski, Raizen et al. 2016). Neuronal
325 and muscular electrical activity leading to pharyngeal contractions can be monitored non-invasively by
326 electropharyngeogram (EPG) recording (Raizen and Avery 1994). An EPG contains transients reflecting
327 pharyngeal muscle action potentials (Figure 8B), the frequency of which can be easily quantified. In the

presence of 10 mM serotonin required to maintain regular pharyngeal pumping, its frequency in the dark was not significantly different in the transgene and wild-type worms (4.07 ± 0.05 and 4.19 ± 0.08 Hz, respectively, mean ± SEM, n = 26 transgenic and 11 wild-type worms, respectively; the p-value by the two-tailed Mann-Whitney test is 0.21), indicating that *Ans*ACR expression did not affect the pharyngeal function in the darkness. Figure 8C shows representative EPG recordings from a transgenic worm fed on bacteria supplemented with all-*trans*-retinal. The onset of 470-nm illumination caused an immediate inhibition of pumping in such transgene worms but not in the WT worms fed on the same bacteria or transgene worms in the absence of retinal (Figure 8D). The *C. elegans* genome encodes LITE-1 and GUR-3 UV/blue light receptors (unrelated to ChRs) responsible for photoinhibition of pharyngeal pumping at high light levels (Bhatla, Droste et al. 2015). However, no photoinhibition was detected in the absence of retinal in either wild-type or transgenic worms. This indicates that the irradiance used in our experiments was insufficient to stimulate these endogenous photoreceptors. The magnitude of the *Ans*ACR-mediated photoinhibition depended on the irradiance (Figure 8E). The maximal irradiance (2.1 mW mm^{-2}) completely abolished the pumping for 15 s in all tested worms (n = 13). In five of 13 worms, individual action potentials were observed during the second half of the 30-s illumination period, an indication of adaptation. Two independently created transgenic lines showed the same degree of photoinhibition (Figure 8E, filled and empty symbols). The photoinhibition was fully reversible: after switching off the maximal-irradiance light, the pumping frequency returned to the pre-illumination level with τ ~9 s.

Discussion

ChRs, also known as "*Chlamydomonas* sensory rhodopsins," were first discovered as the photoreceptors guiding phototaxis and the photophobic response in the chlorophyte *C. reinhardtii* (Sineshchekov, Jung et al. 2002, Govorunova, Jung et al. 2004). Since then, ChRs have been identified in the genomes and transcriptomes of several other eukaryotic supergroups, including cryptophytes, haptophytes, stramenopiles, and alveolates (Govorunova, Sineshchekov et al. 2015, Govorunova, Sineshchekov et al. 2020, Govorunova, Sineshchekov et al. 2021). Furthermore, ChRs appear in the genomes of giant viruses, which likely facilitate the spread of ChR genes by horizontal transfer (Rozenberg, Oppermann et al. 2020, Zabelskii, Alekseev et al. 2020). Our identification and characterization of ChRs in ancyromonads, phylogenetically placed near the most commonly inferred root of the eukaryote tree (Brown, Heiss et al. 2018), suggests that eukaryotes acquired ChR genes at the early steps of their evolution. Consistent with the role of the encoded proteins as phototaxis receptors as shown in *C. reinhardtii*, ChR genes or transcripts have been found only in protists that develop flagella at some stage of their life cycle. The diatom *O. aurita*, in which we identified ChRs, is no exception: the flagella are lost in the vegetative state of this protist but are still present in its male gametes (Nanjappa, Sanges et al. 2017).

Prediction of biophysical properties such as ionic selectivity from protein sequences is a major unresolved problem in ChRs research. The *Nl*CCR sequence shows ~29% identity and ~49% similarity in the 7TM domain to each of the two ancyromonad ACRs and contains a neutral residue in the counterion position (Asp85 in BR), typical of all ACRs (Figure 1 – figure supplement 1, red arrow). Yet, *Nl*CCR does not conduct anions, showing instead permeability to Na^+. In the earlier known ChRs, the presence of conserved Glu residues in TM2 and the TM2-TM3 loop, corresponding to Glu82, Glu83, Glu90, and Glu101 of *Cr*ChR2, correlates with cation selectivity (Govorunova, Sineshchekov et al. 2021). However, TM2 of *Nl*CCR contains no carboxylated residues (Figure 1 – figure supplement 1), which suggests a unique mechanism of cation selection in this channel. *Nl*CCR is the most blue-shifted among ancyromonad ChRs and generates larger photocurrents than the earlier known *Ps*ChR2 with a similar absorption maximum (Govorunova,

371 Sineshchekov et al. 2013), which makes *Nl*CCR a good candidate for optogenetic stimulation of neuronal
372 activity with blue light.

373 All ancyromonad ChRs absorb light in the blue spectral range. The λ_{max} of retinylidene proteins is
374 determined by the energy gap between the electronic ground (S0) and first excited (S1) state of the
375 chromophore and depend on the chromophore geometry, the protonation state of the Schiff base
376 counterion, and the interaction of the chromophore with other residues of the retinal-binding pocket
377 (Ernst, Lodowski et al. 2014, Engqvist, McIsaac et al. 2015, Kato, Kamiya et al. 2015). Paradoxically, the
378 retinal-binding pockets of all three ancyromonad ChRs contain the residues corresponding to Met118 and
379 Ala215 of bacteriorhodopsin, the well-known "color switches" characteristic of red-shifted microbial
380 rhodopsins. The role of the near-ring Met118 homolog in red-shifting the spectrum has been
381 experimentally verified in *Haloquadratum walsbyi* BR (Sudo, Okazaki et al. 2013), *Gloeobacter violaceus*
382 rhodopsin (Engqvist, McIsaac et al. 2015), archaeorhodopsin-3 (Kato, Kamiya et al. 2015), and Chrimson
383 (Oda, Vierock et al. 2018). It is thought that the bulky Met side chain pushes away the C7 atom of retinal,
384 increasing the ring-chain coplanarity, expanding the π-conjugation, and red-shifting absorbance, as
385 theoretically predicted in the *Gt*ACR1_C133M mutant (Tsujimura, Noji et al. 2021). The red-shifting effect
386 of the Ala215 homolog has been demonstrated in *N. pharaonis* sensory rhodopsin II (Shimono, Iwamoto
387 et al. 2000), *H. salinarum* BR (Spudich, Ozorowski et al. 2012), Chrimson (Oda, Vierock et al. 2018), sodium-
388 pumping rhodopsin KR2 (Inoue, Del Carmen Marin et al. 2019), and *Mantoniella squamata* ACR1
389 (Oppermann, Rozenberg et al. 2024), and is explained by electrostatic interactions between the polar
390 residue in this position and the RSB. However, in ancyromonad ChRs, mutations of the Met118 homolog
391 to smaller residues and the Ala215 homolog to polar residues caused a red spectral shift or no shift.
392 Furthermore, the mutagenetic introduction of the ring-rotating residues responsible for the blue-shifted
393 spectra of *Hyphochytrium catenoides* kalium channelrhodopsin 2 (*Hc*KCR2) (Tajima, Kim et al. 2023) and
394 *Kn*ChR (Wang, Natsume et al. 2025) did not change the ancyromonad ChR spectra, which suggests that
395 either the torsion around the C6-C7 bond is already enforced by a different geometry of the Met118
396 homolog or that the blue-shifted absorbance of ancyromonad ChRs arises by a different mechanism.
397 Atomic structures of ancyromonad ChRs are needed to investigate the unexpected spectral shifts we
398 observed when mutating residues of the retinal binding pocket.

399 ACRs are widely used to inhibit neuronal activity with light. We evaluated *Ans*ACR and *Ft*ACR as neuronal
400 silencers in mouse brain slices and *Ans*ACR in the context of a live animal, the nematode *C. elegans*. We
401 previously showed that *Gt*ACRs could inhibit action potentials at the soma while triggering synaptic
402 transmission due to high axonal Cl^- reversal potential (Messier, Chen et al. 2018). *Ans*ACR and *Ft*ACR
403 showed similar phenomena in our brain slice experiments. These ACRs can inhibit action potentials in
404 cortical neurons but depolarize axonal terminals and trigger synaptic transmission at the onset of light
405 stimulation. Fusing these new ACRs with somatodendritic trafficking motifs to reduce axonal expression
406 (Mahn, Gibor et al. 2018, Messier, Chen et al. 2018) could lead to potent inhibition with reduced axonal
407 excitation. Nevertheless, this undesired excitatory effect needs to be taken into consideration when using
408 ACRs.

409 Optogenetic inhibition of *C. elegans* pharyngeal pumping has been demonstrated earlier upon expression
410 of the *Leptosphaeria maculans* proton-pumping rhodopsin known as Mac (Trojanowski, Padovan-Merhar
411 et al. 2014) or *N. pharaonis* halorhodopsin (*Np*HR) (Schuler, Fischer et al. 2015) in the cholinergic neurons.
412 However, ion-pumping rhodopsins such as these transport only one ion per absorbed photon and,
413 therefore, require almost 20 times higher irradiance for photoinhibition than the maximal irradiance used

414 in this study. All ACRs, including *Ans*ACR that we tested in the worms, transport multiple anions during the
415 open state and, therefore, are more efficient optogenetic silencers than the ion-pumping rhodopsins. One
416 possible explanation of the partial recovery of pharyngeal pumping that we observed after 15-s
417 illumination, even at the highest tested irradiance, is continued attenuation of photocurrent during
418 prolonged illumination (desensitization). However, the rate of *Ans*ACR desensitization (Figure 1 – figure
419 supplement 4A and Figure 1 – figure supplement 5A) is much faster than the rate of the pumping recovery,
420 reducing the likelihood that desensitization is driving this phenomenon. Another possible reason for the
421 observed adaptation is an increase in the cytoplasmic Cl^- concentration owing to *Ans*ACR activity and
422 hence a breakdown of the Cl^- gradient on the neuronal membrane. The *C. elegans* pharynx is innervated
423 by 20 neurons, 10 of which are cholinergic (Pereira, Kratsios et al. 2015). A pair of MC neurons is the most
424 important for regulation of pharyngeal pumping, but other pharyngeal cholinergic neurons, including I1,
425 M2, and M4, also play a role (Trojanowski, Padovan-Merhar et al. 2014). Moreover, the pharyngeal
426 muscles generate autonomous contractions in the presence of acetylcholine tonically released from the
427 pharyngeal neurons (Trojanowski, Raizen et al. 2016). Given this complexity, further elucidation of
428 pharyngeal pumping adaptation mechanisms is beyond the scope of this study.

429 In summary, our characterization of ancyromonad channelrhodopsins (ChRs) reveals that their blue-
430 shifted spectral sensitivity and unique ionic selectivity arise from distinct residue motifs not found in
431 previously characterized ChRs. These findings broaden our understanding of how protein sequence
432 modulates light-gated channel function. The blue-shifted absorption properties of ancyromonad ChRs hold
433 promise for multiplexed applications alongside red-shifted indicators and warrant further evaluation
434 across diverse experimental systems.

435 **Materials and Methods**

436 *Bioinformatics and molecular biology*

437 The ChR homologs from *Ancyromonas sigmoides* strain B-70 (CCAP1958/3), *Fabomonas tropica* strain
438 NYK3C, *Nutomonas longa* strain CCAP 1958/5 (Torruella, de Mendoza et al. 2015, Brown, Heiss et al. 2018),
439 and *Ancoracysta twista* strain TD-1 (Janouškovec, Tikhonenkov et al. 2017) were identified in the EukProt
440 V3 database (Richter, Berney et al. 2022) using Sequnceserver BLASTP (Priyam, Woodcroft et al. 2019).
441 The *A. sigmoides*, *F. tropica*, and *A. twista* ChR sequences are also available from Dr. Andrey Rozenberg's
442 ChR database (Rozenberg 2024). The metagenomic homolog 1 was found by Sequnceserver BLASTP in the
443 TARAeuCatV2 database (Sunagawa, Coelho et al. 2015) accessed at the KAUST Metagenomic Analysis
444 Platform (KMAP) (Alam, Kamau et al. 2021). The metagenomic homolog 2 was found using the search
445 mode of BLASTP in the MATOU database (Marine Atlas of Tara Oceans Unigene plus metaG eukaryotes)
446 (Villar, Vannier et al. 2018) with the query sequence of *Nl*CCR. The *Odontella aurita* strain CCMP816
447 homologs GHBW01284417 and GHBW01118808 were identified by TBLASTN in the National Center of
448 Biological Information (NCBI) transcriptome shotgun assembly (TSA) project GHBW00000000. The
449 *Paraphysoderma* homolog (*Pars*R) was found in the *P. sedebokerense* strain JEL821 v. 1.0 genome assembly
450 (Amses, Simmons et al. 2022) by the annotation text search using bacteriorhodopsin as a keyword at the
451 Mycocosm portal (Ahrendt, Mondo et al. 2023).

452 The protein alignment was created using the MUSCLE algorithm with default parameters implemented in
453 MegAlign Pro software v. 17.1.1 (DNASTAR Lasergene, Madison, WI) and truncated after the end of TM7.
454 Phylogeny was analyzed with IQ-TREE v. 2.1.2 (Minh, Schmidt et al. 2020) using automatic model selection
455 and ultrafast bootstrap approximation (1,000 replicates) (Hoang, Chernomor et al. 2018). The best tree

456 was visualized and annotated using iTOL v. 7 (Letunic and Bork 2024). PyMol (v. 2.4.1, Schrödinger) was
457 used for molecular visualization.

458 For expression in human embryonic kidney (HEK293) cells, mammalian codon-optimized polynucleotides
459 encoding amino acid residues 1-265 of the *A. sigmoides* homolog, 1-268 of the *F. tropica* homolog, 1-272
460 of the *N. longa* coding homolog, 1-243 of the *A. twista* homolog, 1-241 of the GHBW01284417 *O. aurita*
461 homolog, 1-242 of the GHBW01118808 *O. aurita* homolog, and 1-336 of the *P. sedebokerense* homolog
462 were synthesized, fused to a C-terminal mCherry tag, and cloned into the pcDNA3.1(+) vector (Invitrogen,
463 Cat. #V19520) at GenScript. Mammalian codon-optimized polynucleotides encoding amino acid residues
464 1-295 of *Gt*ACR1 (Genbank Acc. #KP171708), 1-291 of *Gt*ACR2 (Genbank Acc. #KP171709), and 1-350 of
465 *Chlamydomonas noctigama* ChR1 known as Chrimson (Genbank Acc. #KF992060) were fused to a C-
466 terminal EYFP (enhanced yellow fluorescent protein) tag and cloned into the same vector backbone. For
467 expression in *Pichia*, the constructs were fused with the C-terminal 8His-tag and cloned in the pPICZalpha-
468 A vector (Invitrogen, Cat. #V19520). A QuikChange XL site-directed mutagenesis kit (Agilent Technologies,
469 Cat. #200516) was used to introduce point mutations. For expression in the mouse cortical neurons,
470 *Ans*ACR and *Ft*ACR were tagged with EYFP at the C-terminus and cloned into the pAAV-CAG vector.

471 *HEK293 cell culture and transfection*

472 No cell lines from the list of known misidentified cell lines maintained by the International Cell Line
473 Authentication Committee were used in this study. HEK293 cells used in one-photon (1P) excitation
474 experiments were obtained from the American Type Culture Collection (ATCC, Cat. #CRL-1573). The cells
475 were plated on 2-cm diameter plastic dishes 48-72 hrs before experiments, grown for 24 hrs, and
476 transfected with 10 µl of Lipofectamine LTX with Plus Reagent (ThermoFisher, Cat. #15338100) using 3 µg
477 DNA per dish for manual patch clamping, and 6 µg DNA per dish for automated patch clamping. All-*trans*-
478 retinal (Millipore-Sigma, Cat. #116-31-4) was added immediately after transfection at the final
479 concentration of 5 µM.

480 For 2P excitation experiments, HEK293A cells (Invitrogen, Cat. # R70507) were plated on 30-70 kDa poly-
481 *d*-lysine-coated 12-mm circular coverslips (Carolina cover glass #0, Cat. #633009) in 24-well plates (P24-
482 1.5H-N, Cellvis) at 30% confluence, transfected with 1.2 µL FuGENE HD transfection reagent (Promega, Cat.
483 #E2311) using 200 ng DNA per well 48-72 h before measurements, and supplemented with all-*trans*-
484 retinal as described above.

485 *Automated whole-cell patch clamp recording from HEK293 cells*

486 Automated patch clamp recording was conducted at room temperature (21°C) with a SyncroPatch 384
487 (Nanion Technologies) based on a Biomek i5 automated liquid handler (Beckman Coulter), using NPC-384T
488 S-type chips (Nanion, Cat. #222101) with one hole per well, as described earlier (Govorunova,
489 Sineshchekov et al. 2022). Transfected cells (48-72 h after transfection) were dissociated using TrypLE
490 Express, diluted with CHO-S-SFM-II medium (both from ThermoFisher, Cat.# 12604013 and 31033020,
491 respectively), and resuspended in External Physiological solution (Nation, Cat.# 08 3001). The
492 compositions of this and other solutions used in automated patch clamp recordings and the corresponding
493 liquid junction potential (LJP) values calculated using the ClampEx LJP calculator are listed in
494 Supplementary File 1. The voltages in all IV curves for HEK293 cells studied under 1P excitation in this
495 manuscript were corrected for LJPs; the holding voltage values in the figures showing traces correspond
496 to the amplifier output before the LJP subtraction. Illumination was provided with LUXEON Z Color Line

497 light-emitting diodes (LEDs) Cat.# LXZ1-PB01 (470 ± 10 nm) arranged in a 6×16 matrix. The forward LED
498 current was 900 mA (which corresponded to the irradiance of ~2 mW mm^{-2}), the illumination duration was
499 200 ms (limited by the LED duty cycle), and the interval between successive light pulses was 60 s. The LEDs
500 were driven by a derivative of CardioExcyte 96 SOL (Nanion, Cat. #191003) and controlled by Biomek
501 commands. PatchControl384 v. 2.3.0 (Nanion Technologies) software was used for data acquisition at a 5
502 kHz sampling rate (200 µs per point). The photocurrent amplitudes at the peak and the end of illumination
503 were calculated using DataControl384 software v. 2.3.0 (Nanion Technologies). Further analysis was
504 performed using the Origin Pro 2016 software (OriginLab Corporation).

505 *Manual patch clamp recording using 1P excitation in HEK293 cells*

506 Manual patch clamp recordings were performed with an Axopatch 200B amplifier (Molecular Devices).
507 The pipette solution contained (in mM) KCl 130, MgCl2 2, HEPES 10 pH 7.4, and the bath solution contained
508 (in mM) NaCl 130, $CaCl_2$ 2, $MgCl_2$ 2, glucose 10, HEPES 10 pH 7.4. In experiments to test the relative
509 permeability of ChRs for Cl^-, NaCl in the bath was replaced with Na aspartate, and in experiments in cells
510 co-transfected with *Ans*ACR and Chrimson, KCl in the pipette solution was replaced with K gluconate. The
511 low-pass filter of the amplifier output was set to 2 kHz. The signals were digitized with a Digidata 1440A
512 (Molecular Devices) at a 250-kHz sampling rate (4 µs per point) in experiments with laser flashes, and at a
513 5-kHz sampling rate (200 µs per point) in experiments with continuous light pulses using pClamp 10.7.
514 Patch pipettes with 2-3 MΩ resistances were fabricated from borosilicate glass. Laser excitation was
515 provided by a Minilite Nd:YAG laser (532 nm, pulse width 6 ns, energy 5 mJ; Continuum). The current
516 traces were logarithmically filtered using Logpro software (Spudich 2022). Curve fitting was performed
517 using Origin Pro software. Continuous light pulses were provided by a Polychrome V light source (T.I.L.L.
518 Photonics GMBH) in combination with a mechanical shutter (Uniblitz Model LS6, Vincent Associates; half-
519 opening time 0.5 ms). The action spectra of photocurrents were constructed by calculating the initial slope
520 of photocurrent recorded in response to 15-ms light pulses at the intensity <25 µW mm^{-2}, corrected for
521 the quantum density measured at each wavelength, and normalized to the maximal value. To analyze the
522 dependence of photocurrents on the photon flux density, 1-s light pulses were applied with 60-s dark
523 intervals starting from the lowest density. Calibrated neutral density filters (Newport, Cat. #FSQ-OD50,
524 #FSQ-OD100, #FSQ-OD150, and #FSQ-OD200) were used to adjust the density.

525 *Manual patch clamp recording using 2P excitation in HEK293A cells*

526 2P excitation of *Ans*ACR, *Ft*ACR, *Nl*CCR, *Gt*ACR1, and *Gt*ACR2 expressed in HEK293A cells was conducted
527 using an inverted microscope with multiphoton capability (A1R-MP, Nikon Instruments) at room
528 temperature (23°C). A coverslip seeded with the transfected cells was placed in a custom glass-bottom
529 chamber based on Chamlide EC (Live Cell Instrument) with a glass bottom made with a 24×24 mm cover
530 glass #1 (Erie Scientific, Cat. #89082-270). Cells were perfused continuously with the external solution as
531 described in the 1P excitation section. Whole-cell voltage-clamp recordings were performed using a
532 MultiClamp 700B amplifier (Molecular Devices). Cells were held at −20 mV for power dependency and
533 spectral measurements, and at +20 mV for desensitization measurements. The holding voltages were
534 compensated for the 4.4 mV LJP calculated using the ClampEx v.11.1 (Molecular Devices) built-in
535 calculator. The signals were digitized with an Axon Digidata 1550B1 Low Noise system with a HumSilencer
536 (Molecular Devices), and the current was recorded at 10 kHz using pClamp. The near-IR excitation was
537 generated by a titanium:sapphire femtosecond laser (Chameleon Ultra II, Coherent) with a repetition rate
538 of 80 MHz and a tuning range between 680 and 1,080 nm. Laser pulses were not pre-compensated for

539 dispersion in the microscope optical path. Laser power was tuned using an acousto-optic modulator and
540 delivered to the sample plane through a 40×0.95-numerical aperture (NA) objective (CFI Plan Apochromat
541 Lambda, Nikon Instruments). Scanning across 40.96×40.96 µm regions-of-interest was achieved using
542 resonant scanning at 33.3 Hz.

543 To determine the 2P action spectra of *Ans*ACR, *Ft*ACR, and *Nl*CCR, the excitation wavelength was varied
544 from 800 to 1,080 nm in 40-nm increments. At each wavelength, the laser power at the sample plane was
545 adjusted to 7.5 mW for *Ans*ACR, 5 mW for *Ft*ACR, and 3 mW for *Nl*CCR, as measured using a microscope
546 slide power sensor (S170C, Thorlabs). Excitation power levels were selected to elicit robust photocurrents
547 while minimizing ChR desensitization, by operating at or near the quadratic regime, where doubling the
548 excitation power results in an approximate fourfold increase in the initial photocurrent slope. Deviations
549 from the target power level were kept below 10% and corrected by considering the quadratic dependence
550 of photocurrents on power under 2P excitation. Illumination consisted of 30 consecutive raster scans (total
551 duration ~1 s) over a 40.96×40.96 µm region (512x512 pixels), approximating the average size of a
552 HEK293A cell. Scans were performed back-to-back without temporal gaps, except for the brief interval
553 required for the laser to return to the starting scan position. To mitigate desensitization, we spaced
554 illumination pulses ~54 s apart. We verified that the power ramp and spectral scan protocols caused a less
555 than 20% reduction in the peak photocurrent, as measured at the beginning and end of each protocol
556 using peak-wavelength light pulses at 7.5 mW for *Ans*ACR, 5 mW for *Ft*ACR, and 3 mW for *Nl*CCR. The 2P
557 action spectra were constructed by measuring the initial linear slope of the photocurrent rise at each
558 wavelength and plotted using Origin Pro 2016 software.

559 For desensitization experiments, cells expressing *Ans*ACR, *Ft*ACR, *Nl*CCR, *Gt*ACR1, and *Gt*ACR2 were
560 illuminated near their respective peak wavelengths: *Ans*ACR (920 nm), *Ft*ACR (960 nm), *Nl*CCR (920 nm),
561 *Gt*ACR1 (1040 nm), and *Gt*ACR2 (940 nm) at 15 mW for 5 s. Current traces were low-pass filtered at 100 Hz
562 and, for presentation purposes, downsampled by substituting an average value for each 100 data points.
563 The *Ft*ACR trace was additionally smoothed by the 5-point Savitzky-Golay algorithm in Origin. Peak
564 currents were quantified as the maximal currents over the 5-sec traces. End currents were calculated as
565 the mean current over the final 0.1 s of the 5-sec photoactivation pulse.

566 *Expression and purification of ancyromonad ACRs from Pichia pastoris*

567 The plasmids carrying the expression constructs were linearized with Sac I and delivered into the *P. pastoris*
568 strain SMD1168 (ThermoFisher, Cat. # C17500) by electroporation. A single colony resistant to 0.25 mg/ml
569 zeocin (ThermoFisher, Cat. #R25001) was picked and inoculated into buffered complex glycerol medium,
570 after which the cells were transferred to buffered complex methanol (0.5%) medium supplemented with
571 5 µM all-*trans*-retinal (Millipore-Sigma, Cat. #116-31-4) and grown at 30 °C with shaking at 230 rpm. After
572 24 h, the yellow-colored cells were harvested by centrifugation at 5000 g for 10 min, and the cell pellets
573 were resuspended in 100 ml ice-cold buffer A (20 mM HEPES, pH 7.4, 150 mM NaCl, 1 mM EDTA, 5%
574 glycerol) and lysed by either French press or bead beater. After centrifugation at low speed (5000 g for
575 10 min) to remove cell debris, membrane fractions were pelleted at 190,000 g for 1 h using a Ti45 Beckman
576 rotor. The membranes were suspended in Buffer B (350 mM NaCl, 5% glycerol, 20 mM HEPES, pH 7.5) with
577 1 mM phenylmethylsulfonyl fluoride and solubilized with 1% n-dodecyl-β-D-maltoside (DDM; Anatrace,
578 Cat. # D310) for 1 h at 4 °C with shaking. Undissolved content was removed after ultracentrifugation using
579 a Ti45 rotor at 110,000 g for 1 h. The supernatant supplemented with 15 mM imidazole was incubated
580 with nickel-nitrilotriacetic acid resin (Qiagen, Cat. # 30210) for 1 h with shaking at 4 °C. The resin was

581 washed step-wise using 15 mM and 40 mM imidazole in Buffer B supplemented with 0.03% DDM. The
582 protein was eluted with 400 mM imidazole and 0.03% DDM in buffer B. Protein fractions were pooled and
583 concentrated using a 50 kDa MWCO Amicon Ultra Centrifugal Filter (Millipore-Sigma, Cat. # UFC9050),
584 flash-frozen in liquid nitrogen and stored at −80 °C until use.

585 *Absorption spectroscopy and flash photolysis*

586 Absorption spectra of detergent-purified protein samples were recorded using a Cary 4000
587 spectrophotometer (Varian). Photoinduced absorption changes were measured with a laboratory-
588 constructed crossbeam apparatus. Excitation flashes were provided by a Minilite II Nd:YAG laser (532 nm,
589 pulse width 6 ns, energy 5 mJ; Continuum). Measuring light was from a 250-W incandescent tungsten
590 lamp and a McPherson monochromator (model 272, Acton). Absorption changes were detected with a
591 Hamamatsu Photonics photomultiplier tube (model R928) combined with a second monochromator of
592 the same type. Signals were amplified by a low noise current amplifier (model SR445A; Stanford Research
593 Systems) and digitized with a GaGe Octopus digitizer board (model CS8327, DynamicSignals LLC), with a
594 maximal sampling rate of 50 MHz. Logarithmic data filtration was performed using the GageCon program
595 (Sineshchekov, Govorunova et al. 2023).

596 *Mice*

597 All procedures to maintain and use mice were approved by the Institutional Animal Care and Use
598 Committee at Baylor College of Medicine (protocol AN-6544). Mice were maintained on a 14 hr:10 hr
599 light:dark cycle with regular mouse chow and water ad libitum. The temperature was maintained at 21–
600 25°C and humidity at 40-60%. Experiments were performed during the light cycle. Female ICR (CD-1) mice
601 were purchased from Baylor College of Medicine Center for Comparative Medicine, and male C57BL6/J
602 (JAX #000664) mice were obtained from Jackson Laboratory. Both male and female mice were used in the
603 experiments.

604 *In utero electroporation*

605 Female ICR mice were crossed with male C57BL6/J mice to obtain timed pregnancies. *In utero*
606 electroporation was used to deliver the transgenes (Xue, Atallah et al. 2014). To express *Ans*ACR or *Ft*ACR
607 in the layer 2/3 pyramidal neurons of the somatosensory cortex, pAAV-CAG-*Ans*ACR-EYFP or pAAV-CAG-
608 *Ft*ACR-EYFP (2.5 µg μl^{-1} final concentration) was mixed with pCAG-tdTomato (0.1 µg μl^{-1} final
609 concentration) and Fast Green (Sigma-Aldrich, 0.01% final concentration) for injection. On embryonic day
610 15, pregnant mice were anesthetized, and a beveled glass micropipette (tip size 100-µm outer diameter,
611 50-µm inner diameter) was used to penetrate the uterus and the embryo skull to inject ~1.5 µl DNA
612 solution into one lateral ventricle. Five pulses of current (voltage 39 V, duration 50 ms) were delivered at
613 1 Hz with a Tweezertrode (5-mm diameter) and a square-wave pulse generator (Gemini X2, BTX Harvard
614 Bioscience). The electrode paddles were positioned in parallel with the brain's sagittal plane. The cathode
615 contacted the side of the brain ipsilateral to the injected ventricle to target the somatosensory cortex.
616 Transfected pups were identified by the transcranial fluorescence of tdTomato with an MZ10F
617 stereomicroscope (Leica) 1 day after birth.

618 *Brain slice electrophysiology and imaging*

619 Mice were used at the age of 4-6 weeks for acute brain slice electrophysiology experiments. Mice were
620 anesthetized by an intraperitoneal injection of a ketamine and xylazine mix (80 mg kg^{-1} and 16 mg kg^{-1},

621 respectively) and perfused transcardially with cold (0-4°C) slice cutting solution containing 80 mM NaCl,
622 2.5 mM KCl, 1.3 mM NaH_2PO_4, 26 mM $NaHCO_3$, 4 mM $MgCl_2$, 0.5 mM $CaCl_2$, 20 mM *d*-glucose, 75 mM
623 sucrose and 0.5 mM sodium ascorbate (315 mOsm l^{-1}, pH 7.4, saturated with 95% O_2/5% CO_2). Brains were
624 removed and sectioned in the cutting solution with a VT1200S vibratome (Leica) to obtain 300 µm coronal
625 slices. Slices were incubated in a custom-made interface holding chamber containing slice cutting solution
626 saturated with 95% O_2/5% CO_2 at 34°C for 30 min and then at room temperature for 20 min to 10 h until
627 they were transferred to the recording chamber. We performed recordings on submerged slices in artificial
628 cerebrospinal fluid (ACSF) containing 119 mM NaCl, 2.5 mM KCl, 1.3 mM NaH_2PO_4, 26 mM $NaHCO_3$, 1.3
629 mM $MgCl_2$, 2.5 mM $CaCl_2$, 20 mM *d*-glucose and 0.5 mM sodium ascorbate (305 mOsm l^{-1}, pH 7.4,
630 saturated with 95% O_2/5% CO_2, perfused at 3 ml min^{-1}) at 30-32°C. For whole-cell recordings, a K^+-based
631 pipette solution containing 142 mM K^+ gluconate, 10 mM HEPES, 1 mM EGTA, 2.5 mM $MgCl_2$, 4 mM ATP-
632 Mg, 0.3 mM GTP-Na, 10 mM Na_2-phosphocreatine (295 mOsm l^{-1}, pH 7.35) was used. Membrane
633 potentials reported in Figure 7 and Figure 7 – figure supplement 1 were not corrected for LJP, which was
634 12.5 mV as measured experimentally. Neurons were visualized with video-assisted IR differential
635 interference contrast imaging, and fluorescent neurons were identified by epifluorescence imaging under
636 a water immersion objective (×40, 0.8 NA) on an upright SliceScope Pro 1000 microscope (Scientifica) with
637 an IR-1000 CCD camera (DAGE-MTI). Data were acquired at 10 kHz and low-pass filtered at 4 kHz with an
638 Axon Multiclamp 700B amplifier and an Axon Digidata 1440 A Data Acquisition System under the control
639 of Clampex 10.7 (Molecular Devices). Data were analyzed offline using Clampfit (Molecular Devices). For
640 photostimulation, blue light was emitted from a collimated 470 nm light-emitting diode (LED; M470L3,
641 Thorlabs) to stimulate *Ans*ACR- or *Ft*ACR-expressing neurons. The LEDs were driven by a LED driver
642 (Throlabs LEDD1B) under the control of an Axon Digidata 1440 A Data Acquisition System and Clampex
643 10.7. The light was delivered through the reflected light fluorescence illuminator port and the ×40
644 objective.

645 To evaluate the inhibition efficiency, action potentials of *Ans*ACR- or *Ft*ACR-expressing neurons were
646 evoked by injecting a series of 1.5-s depolarizing current pulses (-0.1-0.5 nA) in whole-cell current clamp
647 mode. 1-s 470 nm (38.7 mW mm^{-2}) light stimulation was applied in the middle of current injections with
648 30-s inter-trial-interval. Resting membrane potentials, input resistances, and capacitances were measured
649 in the trials with -0.1 nA current injection. To examine the excitatory effect of the ACRs, 10-ms 470 nm
650 (38.7 mW mm^{-2}) light stimulation was applied, and ACR^- neurons were clamped at -70 mV to record
651 excitatory post-synaptic currents.

652 After electrophysiology recordings, fluorescent images of the brain slices were acquired on an Axio
653 Zoom.V16 Fluorescence Stereo Zoom Microscope (Zeiss) and processed using MATLAB2024b
654 (MathWorks). Images were taken from 20 brain slices of two male and two female mice.

655 *Generation of transgenic C. elegans strains and EPG recording*

656 The transgenic *C. elegans* strains COP2831 and COP2832 [*uncp*-17::*Ans*ACR::EYFP::*tbb-2u*], *unc-119*(+))} II;
657 *unc-119(ed3)* III expressing *Ans*ACR in cholinergic neurons were created by InVivo Biosystems using the
658 Mos1-mediated Single Copy Insertion (MosSCI) method, which enables integrating the transgene as a
659 single-copy insertion at a designated locus in the *C. elegans* genome (Frokjaer-Jensen 2015). *Unc*-119
660 rescue cassette insertion was used to bring the transgene into a Mos1 target locus on chromosome II and
661 create rescue of the function of the *unc-119(ed3)* III mutant allele. The Mos1 locus was selected for

662 position-neutral effects and to avoid the gene coding regions, introns, and transcription factor binding
663 sites. The integration of the transgene was confirmed by PCR.

664 The transgenic and Bristol N2 wild-type worms were grown at 20°C on *E. coli* strain OP50 lawns in the
665 absence or presence of 10 µM (final concentration) all-*trans*-retinal (Millipore-Sigma, Cat. # 116-31-4),
666 which was mixed with the bacteria before seeding Nematode Growth Medium (NGM) plates. EPG
667 recordings were performed from intact worms sucked into a pipette (Raizen and Avery 1994). The pipettes
668 (200 kΩ resistance) were pulled from borosilicate glass and filled with the External Physiological solution,
669 the composition of which is specified in the above section. The worms were transferred to the same
670 solution supplemented with 10 mM serotonin before the measurements. The data were acquired in the
671 voltage clamp mode of the same Axopatch 200B amplifier used for manual patch clamp recording from
672 HEK293 cells and the same software. The data obtained in two independently created strains were pooled
673 together. The photoexcitation was provided by the Polychrome V light source described above. The
674 frequency of the R1-spikes was calculated using the Event Detection by the Threshold Search function of
675 ClampFit after applying a 2-Hz high-pass digital filter. Further analysis was performed using the Origin Pro
676 2016 software.

677 *Reproducibility and statistics*

678 Plasmids encoding different ChR variants were randomly assigned to transfect identical cell batches. Three
679 independent transfections were performed on different experimental days; the data obtained were pooled
680 together. In automated patch clamp studies, cells were blindly selected by the machine and randomly
681 drawn into the wells. For an unbiased estimation of the photocurrent amplitude, the data from wells that
682 formed seals with a resistance <500 MΩ were excluded. For a more accurate estimation of the V_r values
683 by plotting the IV curves, wells with a seal resistance <500 MΩ and photocurrents of the absolute
684 magnitude <50 pA at -80 mV were excluded. In manual patch clamp experiments, the cells were selected
685 for patching by inspecting their tag fluorescence; non-fluorescent cells and cells in which no GΩ seal was
686 established or lost during recording were excluded from the analysis. Recordings with the access resistance
687 (R_a) >20 MΩ were excluded from the analysis. In automated and manual patch clamp experiments, the
688 photocurrent traces recorded from different cells transfected with the same construct were considered
689 biological replicates (reported as n values). These values indicate how often the experiments were
690 performed independently. In experiments using continuous light pulses, only one photocurrent trace was
691 recorded from one cell for each condition. To increase the signal-to-noise ratio for computer
692 approximations of the photocurrent traces under single-turnover conditions, six replicates recorded from
693 the same cells were considered technical replicates and averaged for further analysis.

694 Statistical analysis of the patch clamp data was performed using Origin Pro 2016 software. The normal
695 distribution of the data was not assumed. The non-parametric two-tailed Mann-Whitney and Kolmogorov-
696 Smirnov tests were used to compare the means. No statistical methods were used to pre-determine
697 sample sizes, but the sample sizes were similar as those reported in the previous publications
698 (Govorunova, Gou et al. 2022, Morizumi, Kim et al. 2023).

699 In the cortical neuron patch clamp experiments, fluorescently labelled or negative neurons were randomly
700 selected from the densely labelled area of brain slices. The criteria for data exclusion were the same as in
701 manual patch clamp recordings from HEK cells. Statistical analysis of the data was performed using
702 ClampFit 10.7 (Molecular Devices) and Prism 10.3 (GraphPad). The multiple Wilcoxon matched-pairs

signed rank test with Benjamini, Krieger, and Yekutieli's corrections was used for evaluating the efficiency of action potential inhibition.

In *C. elegans* experiments, the EPG recordings were excluded from the analysis, if the worm moved out of the illuminated area during recording. No data was excluded in flash photolysis experiments.

Data and materials availability

The numerical data and statistical analyses are provided in the Source Data Files. The sequence information was deposited at the NCBI with GenBank Acc. #PQ657777-PQ657783. The plasmids encoding *Ans*ACR, *Ft*ACR, and *Nl*CCR expression constructs in the pcDNA3.1 vector backbone were deposited at Addgene (plasmids #232598, 232599, and 232600, respectively). The plasmids pAAV-CAG-*Ans*ACR-EYFP and pAAV-CAG-*Ft*ACR-EYFP were deposited at Addgene (plasmids #238347 and #238348, respectively). The recombinant *C. elegans* lines expressing *Ans*ACR in the cholinergic neurons are available from the authors upon request.

Acknowledgments

We thank Dr. Valeria Vasquez (UTHealth) for a generous donation of the wild-type *C. elegans* strain and OP50 *E. coli* strain. We thank Dr. Edward S. Boyden (Massachusetts Institute of Technology) for a gift of the Chrimson plasmid. This work was supported by the National Institutes of Health grants R35GM140838 (J.L.S.), S10OD032293 (J.L.S.), U01NS118288 (M.X., J.L.S., F.S.P.), RF1NS133657 (J.L.S., F.S.P., M.X.), R61CA278458 (F.S.P.), and R01NS136027 (F.S.P.); the Robert A. Welch Foundation Endowed Chair AU-0009 (J.L.S.), and grants Q-2016-20220331 (F.S.P.) and Q-2016-20190330 (F.S.P.); a Vivian L. Smith Endowed Professorship in Neuroscience (F.S.P); the McNair Medical Foundation (F.S.P); the Natural Sciences and Engineering Research Council of Canada (NSERC) grants RGPIN-2018-04397 and RGPIN-2024-03857 (L.S.B.). An NSERC USRA award supported A.P., and S.M. was supported by the President's Research Assistantship (PRA) program at the University of Guelph. M.X. is a Caroline DeLuca Scholar.

Declaration of interests

M.X. was a consultant to Capsida Biotherapeutics. Capsida Biotherapeutics provided research funds to Baylor College of Medicine to support a research project in his lab that is unrelated to this study and had no role in the research, authorship, and publication of this article.

Figure 1. Phylogeny, spectral sensitivity, and light dependence of ancyromonad ChRs.
(**A**) A maximum-likelihood phylogenetic tree of selected ChRs. The circles show bootstrap support from 40 to 100. (**B**) The photocurrent action spectra. The data points are the mean ± SEM values (n = 14 cells for *Ans*ACR, and 9 cells each for *Ft*ACR and *Nl*CCR). (**C**) The absorption spectra of detergent-purified proteins. (**D**) The action spectra of photocurrents at -60 mV upon co-expression of *Ans*ACR and Chrimson, compared to each gene expressed alone. The data points are the mean ± SEM values (n = 14 cells each for the co-expression and *Ans*ACR, and 4 cells for Chrimson). (**E, F**) The dependence of the peak current amplitude (E) and reciprocal time to the peak (F) on the photon flux density for the indicated ChRs activated at their respective λ_{max}. The data points are the mean ± SEM values (n = 8 cells for each variant).

The online version of this article includes the following source data for Figure 1:
Source data 1. Source data for the protein names and accession numbers used to construct the tree in (A); numerical values for the data shown in (B-F).

742 **Figure 2. Characterization of ancyromonad ChRs by automated patch clamping.** (**A-C**) Photocurrent
743 traces recorded in response to 200-ms light pulses (470 nm) at voltages varied in 20-mV steps from -80
744 mV using the KF-based internal and NaCl-based external solutions. The dashed lines show the zero-current
745 level. (**D-F**) The IV curves of the peak photocurrent (filled circles) and the current at the end of illumination
746 (empty circles). The numbers in the parentheses are the numbers of cells sampled. (**G**) Comparison of the
747 V_r at the photocurrent peak time (filled circles) and the end of illumination (empty circles). The p-values
748 were determined by the two-tailed Wilcoxon signed-rank test; the number of cells sampled for each
749 variant was the same as in panels D-F. (**H-J**) The V_r values in the indicated external solutions. The circles
750 are the data from individual cells; the lines are the mean and SEM values.

751 The online version of this article includes the following source data for Figure 2:
752 **Source data 1**. Source data for the numbers of cells sampled and numerical values shown in (D-J).

753 **Figure 3. Photocurrent and transient absorption changes under single-turnover conditions in *Ans*ACR**
754 **and *Ft*ACR.**
755 (**A, D**) Photocurrent traces of *Ans*ACR (A) and *Ft*ACR (D) evoked by 6-ns laser flashes recorded by manual
756 patch clamping at the holding voltages increased in 30-mV steps from -60 mV. (**B, E**) Transient absorption
757 changes recorded at the indicated wavelengths from detergent-purified proteins. (**C, F**) Comparison of the
758 photocurrent kinetics (red, left axis) and the M intermediate kinetics (black, left axis). In all panels, the
759 thin, solid lines are experimental recordings, and the thick, dashed lines are multiexponential
760 approximations. The numbers are the τ values of the individual kinetic components.

761 **Figure 4. Probing the residues in the counterion positions.** (**A**) pH titration of λ_{max} (black filled circles, left
762 axis) and maximal absorption changes (black empty circles, right axis) in wild-type *Ans*ACR. (**B, C**) pH
763 titration of λ_{max} in *Ft*ACR (B) and *Nl*CCR (C). (**D**) The photocurrent action spectrum of the *Ans*ACR_D226N
764 mutant (red) compared to the WT (black). The data points are the mean ± SEM values (n = 8 cells). (**E**)
765 Photocurrent traces of *Ans*ACR_D226N mutant evoked by 6-ns laser flashes recorded by manual patch
766 clamping at the holding voltages increased in 30-mV steps from -60 mV. The wild-type photocurrent trace
767 recorded at -60 mV is shown in black for comparison. The thin lines are experimental recordings, and the
768 thick dashed lines are multiexponential approximations. The numbers are the τ values of the individual
769 kinetic components. (**F**) The voltage dependence of the decay components τ in the *Ans*ACR_D226N mutant
770 (red) and the WT (black). (**G**) pH titration of λ_{max} in *Ans*ACR_G86E mutant. (**H**) Transient absorption changes
771 monitored at the wavelength of the M intermediate absorption in the *Ans*ACR_G86E mutant (red)
772 compared to the WT (black). (**I**) Laser-flash-induced photocurrents of the *Ans*ACR_G86E mutant recorded
773 at the external pH 7.4 (black) and 5.4 (red). The arrow shows the increase in the channel current upon
774 acidification.

775 The online version of this article includes the following source data for Figure 4:
776 **Source data 1**. Source data for the numerical values shown in (A-D, F, and G).

777 **Figure 5. Color tuning of ancyromonad ChRs.**
778 (**A**) Amino acid residues of the retinal-binding pocket tested by mutagenesis in this study. (**B**) The
779 corresponding residues in the *Gt*ACR1 structure (6edq). (**C-K**) The photocurrent action spectra of the
780 indicated mutants compared to the respective WTs. The data points are the mean ± SEM values (the n
781 values are provided in the Source Data 1).

The online version of this article includes the following source data for Figure 5:
Source data 1. Source data for the numbers of cells sampled and numerical values shown in (C-K).

Figure 6. **2P excitation of ancyromonad ACRs.** (**A**) The 2P photocurrent action spectra. The data points are the mean ± SEM values (n = 5 cells for each variant). (**B-F**) The mean normalized photocurrent traces recorded upon 2P excitation from the indicated ChR variants (*Gt*ACR1 and *Gt*ACR2 are included for comparison) at +20 mV in the Cl^--based external solution (n = 6 cells for each variant). The illumination (the duration of which is shown as the bars on top) was 15 mW at the λ_{max} for each variant. (**G, H**) The amplitude of photocurrent measured at the peak time (G) and at the end of 5-s illumination (H). (**I**) Desensitization at the end of illumination. In G-I, the symbols are the data from individual cells, the lines are mean ± SEM values (n = 6 cells for each variant). For more detail see Methods.

The online version of this article includes the following source data for Figure 6:
Source data 1. Source data for the numerical values shown in (A and G-I).

Figure 7. Photoactivation of *Ans*ACR and *Ft*ACR inhibits the action potentials of mouse cortical neurons. (**A, B**) Representative membrane voltage traces of neurons expressing *Ans*ACR (A) and *Ft*ACR (B) in response to -0.1 nA (left), 0 nA (middle), and 0.5 nA (right) injections without (top) and with (bottom) 470 nm light pulses (power density of 38.7 mW mm^{-2}). (**C, D**) The frequencies of action potentials evoked by different current injections with (blue) and without (black) photoactivation of *Ans*ACR (C) and *Ft*ACR (D). For all panels, data points from male mice are indicated by squares and female mice by circles. One male and one female mouse were used for each of the *Ans*ACR and *Ft*ACR experiments. Data are mean ± SEM. **, $p \leq 0.01$ for for comparison between dark and light stimulation at 0.2-0.5 nA current injection by the multiple Wilcoxon matched-pairs signed rank test with Benjamini, Krieger, and Yekutieli's corrections.

The online version of this article includes the following source data for Figure 7:
Source data 1. Source data for the numerical values shown in (C, D).

Figure 8. Photoinhibition of pharyngeal pumping in live *C. elegans* expressing *Ans*ACR in the cholinergic neurons.
(**A**) A scheme of the genetic construct for *Ans*ACR expression in the cholinergic neurons. HA, homology arms. (**B**) A zoomed-in section of an EPG recording. AP, action potential; TB, terminal bulb. The double-headed arrow shows the interval between two successive R1 spikes used to calculate pharyngeal pumping frequency. (**C**) Electropharyngeogram recordings from an *Ans*ACR-expressing worm illuminated with 470 nm light at the indicated irradiances. The blue bar shows the duration of illumination. (**D**) The frequency of the pharyngeal pumping calculated from recordings as shown in A. The symbols are the mean values, and the error bars are the SEM values (n = 11 worms for the WT and 13 worms per condition for the transgenic worms). The numbers are the irradiance values in mW mm^{-2}; ret is retinal. (**E**) The dependence of the pharyngeal pumping frequency on the irradiance calculated from the 30-60 s segment of the data shown in B. The symbols are the data from individual worms; the lines are the mean and SEM values. The empty and filled symbols for the transgenic worms show the data from two independently created transgenic lines.

The online version of this article includes the following source data for Figure 8:
Source data 1. Source data for the numerical values shown in (D, E).

822 **Figure supplement legends**

823 **Figure 1 – figure supplement 1. The protein alignment of the 7TM domains of ChR variants identified**
824 **and characterized in this study and the previously known *Gt*ACR1.**
825 The amino acid residues are colored according to their chemical properties. The residue ruler is according
826 to the *Gt*ACR1 sequence. The lines show the transmembrane helices TM1-TM7 of *Gt*ACR1. The arrows
827 point to the positions corresponding to Asp68 (black), Ser97 (red), and Asp234 (blue) of *Gt*ACR1.

828 **Figure 1 – figure supplement 2. Action spectra and photocurrents of ACRs from *Ancoracysta twista* and**
829 ***Odontella aurita.***
830 In the left panels, the action spectra. The data points are the mean ± SEM values; n = 6 cells for each
831 variant. In the middle and right panels, the photocurrents recorded by manual patch clamping in the Cl^-
832 bath (middle) and Asp^- bath (right) at the holding voltages increased in 20-mV increments from -60 mV.
833 The dark cyan bars show the duration of illumination (500, 520 and 510 nm, respectively, for *At*ACR,
834 *Oa*ACR1, and *Oa*ACR2).

835 **Figure 1 – figure supplement 3. Comparison of the absorption and action spectra of individual**
836 **ancyromonad ChRs.**
837 (**A-C**) Overlays of the absorption and action spectra from the main text Figures 1B and C.

838 **Figure 1 – figure supplement 4. Desensitization at the end of 1-s illumination.**
839 (**A-E**) Normalized photocurrent traces recorded from the indicated ChRs at -60 mV. The colored rectangles
840 show the duration of illumination. The numbers are photon flux densities multiplied by 10^{16}. (**F**) The
841 dependence of desensitization, calculated as the peak minus end current divided by the peak current and
842 multiplied by 100%, on the photon flux density. The data points are mean ± SEM (n = 8 cells for each
843 variant).

844 The online version of this article includes the following source data for Figure 1 – figure supplement 4:
845 **Source data 1**. Source data for the numerical values shown in (F).

846 **Figure 1 – figure supplement 5. Desensitization at the end of 5-s illumination.**
847 (**A-E**) Normalized photocurrent traces recorded from the indicated ChRs at +20 mV. The colored rectangles
848 show the duration of illumination. (**F**) Desensitization at the end of illumination. The symbols are data from
849 individual cells, the lines are mean ± SEM, n = 6 cells for each variant.

850 The online version of this article includes the following source data for Figure 1 – figure supplement 4:
851 **Source data 1**. Source data for the numerical values shown in (F).

852 **Figure 2 – figure supplement 1. Photocurrent amplitudes of anycromonad ChRs and comparison of**
853 ***Nl*CCR with *Cr*ChR2.**
854 (**A, B**) Unbiased estimation of peak photocurrent amplitudes. The photocurrents were recorded at 20 mV
855 for *Ans*ACR and *Ft*ACR, and at -60 mV for *Nl*CCR and *Ps*ChR2. *, p = 0.0047; **, p = 9.9E10-6 by the two-
856 tailed, two-sample Kolmogorov-Smirnov test. (**C, D**) The V_r shifts measured upon replacing Na^+ with
857 $NMDG^+$ in the external solution (C), and upon its acidification from pH 7.4 to 5.4 (D). In all panels, the
858 symbols are the data from individual cells; the lines are the mean and SEM values; the numbers in brackets
859 are the numbers of cells sampled.

The online version of this article includes the following source data for Figure 2 – figure supplement 1:
Source data 1. Source data for the numbers of cells sampled and numerical values shown in (A-D).

Figure 2 – figure supplement 2. Photocurrent traces recorded from ancyromonad ChRs by manual patch clamping.
The photocurrents were recorded by manual patch clamping in the Cl^- bath (left), Asp^- bath (middle), and $NMDG^+$ bath (right) at the holding voltages increased in 20-mV increments from -60 mV. The blue bars show the duration of 470 nm illumination.

Figure 3 – figure supplement 1. Current-voltage relationships of photocurrent kinetic components in the three ancyromonad ChRs and laser-flash-evoked *Nl*CCR photocurrents.
(**A, B,** and **D**). The voltage dependence of the amplitudes of the channel closing and opening components estimated by multi-componential approximation of the laser-flash-evoked photocurrents recorded from the indicated ancyromonad ChRs. (**C**) Laser-flash evoked photocurrent traces of *Nl*CCR recorded at the holding voltages increased in 30-mV steps from -60 mV in the Cl^--based bath (black) and at -60 mV in the Asp^--based bath (red). The thin lines are experimental recordings, and the thick dashed lines are multiexponential approximations. The numbers are the τ values of the individual kinetic components.

The online version of this article includes the following source data for Figure 3 – figure supplement 1:
Source data 1. Source data for the numerical values shown in (A, B, and D).

Figure 4 – figure supplement 1. Dependence of absorption on the Cl^- concentration.
The lines are the absorption spectra of detergent-purified *Ans*ACR at the indicated Cl^- concentrations.

Figure 4 – figure supplement 2. Continued analysis of the *Ans*ACR_G86E mutant.
(**A**) The voltage dependence of the fast current at pH 7.4 (black) and 5.4 (red). (**B**) The voltage dependence of the channel current at pH 5.4 in the Cl^--based bath (black) and the Asp^--based bath (blue). **(C)** The difference spectra obtained upon alkalization on the purified mutant (red) and WT (black). (**D**) pH titration of the absorbance difference at 297 nm in the purified mutant (red) and WT (black).

The online version of this article includes the following source data for Figure 4 – figure supplement 2:
Source data 1. Source data for the numerical values shown in (A, B, and D).

Figure 4 – figure supplement 3. Photocurrents in the *Ans*ACR_Q48E mutant.
(**A**) Laser-flash evoked photocurrent traces of the mutant recorded at the holding voltages increased in 30-mV steps from -60 mV (red). A trace from the WT at -60 mV (black) is shown for comparison. The thin lines are experimental recordings, and the thick dashed lines are multiexponential approximations. The numbers are the τ values of the individual kinetic components. (**B**) The voltage dependence of the amplitudes of the kinetic components obtained by multiexponential approximation of the laser-flash-evoked photocurrents.

Figure 5 – figure supplement 1. Mutations blue-shifting other microbial rhodopsins spectra do not affect ancyromonad ChRs.
The photocurrent action spectra of the indicated mutants compared to the respective WTs. The data points are the mean ± SEM values.

The online version of this article includes the following source data for Figure 5 – figure supplement 1:

898 **Source data 1**. Source data for the numbers of cells sampled and numerical values shown in (A-D).

899 **Figure 6 – figure supplement 1. Power dependence upon 2P illumination.**
900 (**A-C**) The dependence of the photocurrent rise on the quadratic light power. The data points are the mean
901 ± SEM (n = 5 cells for each variant). A 2nd-order polynomial function was fit to the data. The dashed lines
902 show a linear approximation of the initial portion of the curve.

903 **Figure 7 – figure supplement 1. Characterization of *Ans*ACR and *Ft*ACR expression in cortical neurons**
904 **and axonal excitatory effect.**
905 (**A**) Representative fluorescence images of 300 µm-thick brain slices expressing tdTomato and EYFP fused
906 to the C termini of *Ans*ACR (left) and *Ft*ACR (right) in cortical layer 2/3 pyramidal neurons. The axons of
907 ACR$^+$ layer 2/3 pyramidal neurons ramify in layer 5. L, layer. (**B**) Resting membrane potentials (left), input
908 resistances (middle), and capacitances (right) of *Ans*ACR$^+$ and *Ft*ACR$^+$ neurons. (**C**) Representative traces
909 of light-evoked excitatory post-synaptic currents (EPSCs) recorded from ACR$^-$ pyramidal neurons in layer
910 2/3 in response to 10-ms 470 nm light pulses (power density of 38.7 mW mm^{-2}). (**D**) Summary data of
911 experiments in (C). The peak currents of light-evoked EPSCs were measured from the averaged current
912 traces of three trials. In all panels, the data points from male mice are indicated by squares and female
913 mice by circles. One male and one female mouse were used for each of the *Ans*ACR and *Ft*ACR
914 experiments. The data points are the mean ± SEM values.

915 The online version of this article includes the following source data for Figure 6 – figure supplement 1:
916 **Source data 1**. Source data for the numbers of cells sampled and numerical values shown in (B, D).

917 **Supplementary File 1.** Compositions and liquid junction potential (LJP) values of the solutions used in
918 automated patch clamp recording.

919 **Supplementary File 2.** The wavelength positions of the half-maximal amplitude of the long-wavelength
920 slope of the spectrum (λ_{50}) of ChR variants tested in this study.

921

References

Ahrendt, S. R., S. J. Mondo, S. Haridas and I. V. Grigoriev (2023). "MycoCosm, the JGI's fungal genome portal for comparative genomic and multiomics data analyses." Methods Mol Biol **2605**: 271-291.

Alam, I., A. A. Kamau, D. K. Ngugi, T. Gojobori, C. M. Duarte and V. B. Bajic (2021). "KAUST Metagenomic Analysis Platform (KMAP), enabling access to massive analytics of re-annotated metagenomic data." Sci Rep **11**(1): 11511.

Amses, K. R., D. R. Simmons, J. E. Longcore, S. J. Mondo, K. Seto, G. H. Jeronimo, A. E. Bonds, C. A. Quandt, W. J. Davis, Y. Chang, B. A. Federici, A. Kuo, K. LaButti, J. Pangilinan, W. Andreopoulos, A. Tritt, R. Riley, H. Hundley, J. Johnson, A. Lipzen, K. Barry, B. F. Lang, C. A. Cuomo, N. E. Buchler, I. V. Grigoriev, J. W. Spatafora, J. E. Stajich and T. Y. James (2022). "Diploid-dominant life cycles characterize the early evolution of fungi." Proc Natl Acad Sci USA **119**(36): e2116841119.

Bergs, A., T. Henss, C. Glock, J. Nagpal and A. Gottschalk (2022). "Microbial rhodopsin optogenetic tools: Application for analyses of synaptic transmission and of neuronal network activity in behavior." Methods Mol Biol **2468**: 89-115.

Bhatla, N., R. Droste, S. R. Sando, A. Huang and H. R. Horvitz (2015). "Distinct neural circuits control rhythm inhibition and spitting by the myogenic pharynx of *C. elegans*." Curr Biol **25**(16): 2075-2089.

Brown, M. W., A. A. Heiss, R. Kamikawa, Y. Inagaki, A. Yabuki, A. K. Tice, T. Shiratori, K. I. Ishida, T. Hashimoto, A. G. B. Simpson and A. J. Roger (2018). "Phylogenomics places orphan protistan lineages in a novel eukaryotic super-group." Genome Biol Evol **10**(2): 427-433.

Chen, F., X. Duan, Y. Yu, S. Yang, Y. Chen, C. E. Gee, G. Nagel, K. Zhang, S. Gao and Y. Shen (2022). "Visual function restoration with a highly sensitive and fast Channelrhodopsin in blind mice." Signal Transduct. Target Ther. **7**(1): 104.

Chen, W., Z. L. Cai, E. S. Chao, H. Chen, C. M. Longley, S. Hao, H. T. Chao, J. H. Kim, J. E. Messier, H. Y. Zoghbi, J. Tang, J. W. Swann and M. Xue (2020). "Stxbp1/Munc18-1 haploinsufficiency impairs inhibition and mediates key neurological features of STXBP1 encephalopathy." Elife **9**: e48705.

Deisseroth, K. (2021). "From microbial membrane proteins to the mysteries of emotion." Cell **184**(21): 5279-5285.

Doyon, N., L. Vinay, S. A. Prescott and Y. De Koninck (2016). "Chloride regulation: A dynamic equilibrium crucial for synaptic inhibition." Neuron **89**(6): 1157-1172.

Emiliani, V., E. Entcheva, R. Hedrich, P. Hegemann, K. R. Konrad, C. Lüscher, M. Mahn, Z.-H. Pan, R. R. Sims, J. Vierock and O. Yizhar (2022). "Optogenetics for light control of biological systems." Nature Reviews Methods Primers **2**(1): 55.

Engqvist, M. K., R. S. McIsaac, P. Dollinger, N. C. Flytzanis, M. Abrams, S. Schor and F. H. Arnold (2015). "Directed evolution of *Gloeobacter violaceus* rhodopsin spectral properties." J. Mol. Biol. **427**: 205-220.

Ernst, O. P., D. T. Lodowski, M. Elstner, P. Hegemann, L. S. Brown and H. Kandori (2014). "Microbial and animal rhodopsins: structures, functions, and molecular mechanisms." Chem. Rev. **114**(1): 126-163.

Forli, A., D. Vecchia, N. Binini, F. Succol, S. Bovetti, C. Moretti, F. Nespoli, M. Mahn, C. A. Baker, M. M. Bolton, O. Yizhar and T. Fellin (2018). "Two-photon bidirectional control and imaging of neuronal excitability with high spatial resolution in vivo." Cell Rep. **22**(11): 3087-3098.

Frokjaer-Jensen, C. (2015). "Transposon-Assisted Genetic Engineering with Mos1-Mediated Single-Copy Insertion (MosSCI)." Methods Mol Biol **1327**: 49-58.

Govorunova, E. G., Y. Gou, O. A. Sineshchekov, H. Li, X. Lu, Y. Wang, L. S. Brown, F. St-Pierre, M. Xue and J. L. Spudich (2022). "Kalium channelrhodopsins are natural light-gated potassium channels that mediate optogenetic inhibition." Nat. Neurosci. **25**(7): 967-974.

Govorunova, E. G., K.-W. Jung, O. A. Sineshchekov and J. L. Spudich (2004). "*Chlamydomonas* sensory rhodopsins A and B: Cellular content and role in photophobic responses." Biophys. J. **86**: 2342-2349.

Govorunova, E. G., O. A. Sineshchekov, L. S. Brown and J. L. Spudich (2022). "Biophysical characterization of light-gated ion channels using planar automated patch clamp." Front. Mol. Neurosci. **15**: 976910.

Govorunova, E. G., O. A. Sineshchekov, H. Li, R. Janz and J. L. Spudich (2013). "Characterization of a highly efficient blue-shifted channelrhodopsin from the marine alga *Platymonas subcordiformis*." J. Biol. Chem. **288**(41): 29911-29922.

Govorunova, E. G., O. A. Sineshchekov, H. Li, Y. Wang, L. S. Brown, A. Palmateer, M. Melkonian, S. Cheng, E. Carpenter, J. Patterson, G. K. S. Wong and J. L. Spudich (2021). "Cation and anion channelrhodopsins: Sequence motifs and taxonomic distribution." MBio **12**: e0165621.

Govorunova, E. G., O. A. Sineshchekov, H. Li, Y. Wang, L. S. Brown and J. L. Spudich (2020). "RubyACRs, non-algal anion channelrhodopsins with highly red-shifted absorption." Proc. Natl. Acad. Sci. USA **117**: 22833-22840.

Govorunova, E. G., O. A. Sineshchekov, X. Liu, R. Janz and J. L. Spudich (2015). "Natural light-gated anion channels: A family of microbial rhodopsins for advanced optogenetics." Science **349**(6248): 647-650.

Govorunova, E. G., O. A. Sineshchekov and J. L. Spudich (2022). "Emerging diversity of channelrhodopsins and their structure-function relationships." Front Cell Neurosci **15**: 800313.

Govorunova, E. G., O. A. Sineshchekov and J. L. Spudich (2023). "Potassium-selective channelrhodopsins." Biophysics and Physicobiology **20**: e201011.

Hoang, D. T., O. Chernomor, A. von Haeseler, B. Q. Minh and L. S. Vinh (2018). "UFBoot2: Improving the ultrafast bootstrap approximation." Mol. Biol. Evol. **35**(2): 518-522.

Hochbaum, D. R., Y. Zhao, S. L. Farhi, N. Klapoetke, C. A. Werley, V. Kapoor, P. Zou, J. M. Kralj, D. Maclaurin, N. Smedemark-Margulies, J. L. Saulnier, G. L. Boulting, C. Straub, Y. K. Cho, M. Melkonian, G. K. Wong, D. J. Harrison, V. N. Murthy, B. L. Sabatini, E. S. Boyden, R. E. Campbell and A. E. Cohen (2014). "All-optical electrophysiology in mammalian neurons using engineered microbial rhodopsins." Nat. Methods **8**: 825-833.

Hoffmann, M., M. Wanko, P. Strodel, P. H. Konig, T. Frauenheim, K. Schulten, W. Thiel, E. Tajkhorshid and M. Elstner (2006). "Color tuning in rhodopsins: the mechanism for the spectral shift between bacteriorhodopsin and sensory rhodopsin II." J. Am. Chem. Soc. **128**(33): 10808-10818.

Inoue, K., M. Del Carmen Marin, S. Tomida, R. Nakamura, Y. Nakajima, M. Olivucci and H. Kandori (2019). "Red-shifting mutation of light-driven sodium-pump rhodopsin." Nat. Commun. **10**(1): 1993.

Janouškovec, J., D. V. Tikhonenkov, F. Burki, A. T. Howe, F. L. Rohwer, A. P. Mylnikov and P. J. Keeling (2017). "A new lineage of eukaryotes illuminates early mitochondrial genome reduction." Curr Biol **27**(23): 3717-3724 e3715.

1000 Karasuyama, M., K. Inoue, R. Nakamura, H. Kandori and I. Takeuchi (2018). "Understanding colour tuning
1001 rules and predicting absorption wavelengths of microbial rhodopsins by data-driven machine-learning
1002 approach." Sci. Rep. **8**(1): 15580.

1003 Kato, H. E., M. Kamiya, S. Sugo, J. Ito, R. Taniguchi, A. Orito, K. Hirata, A. Inutsuka, A. Yamanaka, A. D.
1004 Maturana, R. Ishitani, Y. Sudo, S. Hayashi and O. Nureki (2015). "Atomistic design of microbial opsin-
1005 based blue-shifted optogenetics tools." Nat. Commun. **6**: 7177.

1006 Kim, Y. S., H. E. Kato, K. Yamashita, S. Ito, K. Inoue, C. Ramakrishnan, L. E. Fenno, K. E. Evans, J. M. Paggi,
1007 R. O. Dror, H. Kandori, B. K. Kobilka and K. Deisseroth (2018). "Crystal structure of the natural anion-
1008 conducting channelrhodopsin *Gt*ACR1." Nature **561**: 343-348.

1009 Letunic, I. and P. Bork (2024). "Interactive Tree of Life (iTOL) v6: recent updates to the phylogenetic tree
1010 display and annotation tool." Nucleic Acids Res **52**(W1): W78-W82.

1011 Li, H., C. Y. Huang, E. G. Govorunova, C. T. Schafer, O. A. Sineshchekov, M. Wang, L. Zheng and J. L.
1012 Spudich (2019). "Crystal structure of a natural light-gated anion channelrhodopsin." Elife **8**: e41741.

1013 Mahn, M., L. Gibor, P. Patil, K. Cohen-Kashi Malina, S. Oring, Y. Printz, R. Levy, I. Lampl and O. Yizhar
1014 (2018). "High-efficiency optogenetic silencing with soma-targeted anion-conducting channelrhodopsins."
1015 Nat. Commun. **9**(1): 4125.

1016 Man, D., W. Wang, G. Sabehi, L. Aravind, A. F. Post, R. Massana, E. N. Spudich, J. L. Spudich and O. Béjà
1017 (2003). "Diversification and spectral tuning in marine proteorhodopsins." EMBO J. **22**: 1725-1731.

1018 Mardinly, A. R., I. A. Oldenburg, N. C. Pegard, S. Sridharan, E. H. Lyall, K. Chesnov, S. G. Brohawn, L. Waller
1019 and H. Adesnik (2018). "Precise multimodal optical control of neural ensemble activity." Nat. Neurosci.
1020 **21**: 881-893.

1021 Messier, J. E., H. Chen, Z. L. Cai and M. Xue (2018). "Targeting light-gated chloride channels to neuronal
1022 somatodendritic domain reduces their excitatory effect in the axon." Elife **7**: e38506.

1023 Minh, B. Q., H. A. Schmidt, O. Chernomor, D. Schrempf, M. D. Woodhams, A. von Haeseler and R. Lanfear
1024 (2020). "IQ-TREE 2: New models and efficient methods for phylogenetic inference in the genomic era."
1025 Mol. Biol. Evol. **37**(5): 1530-1534.

1026 Morizumi, T., K. Kim, H. Li, E. G. Govorunova, O. A. Sineshchekov, Y. Wang, L. Zheng, E. Bertalan, A. N.
1027 Bondar, A. Askari, L. S. Brown, J. L. Spudich and O. P. Ernst (2023). "Structures of channelrhodopsin
1028 paralogs in peptidiscs explain their contrasting K^+ and Na^+ selectivities." Nat Commun **14**(1): 4365.

1029 Nanjappa, D., R. Sanges, M. I. Ferrante and A. Zingone (2017). "Diatom flagellar genes and their
1030 expression during sexual reproduction in Leptocylindrus danicus." BMC Genomics **18**(1): 813.

1031 Oda, K., J. Vierock, S. Oishi, S. Rodriguez-Rozada, R. Taniguchi, K. Yamashita, J. S. Wiegert, T. Nishizawa, P.
1032 Hegemann and O. Nureki (2018). "Crystal structure of the red light-activated channelrhodopsin
1033 Chrimson." Nat. Commun. **9**: 3949.

1034 Oppermann, J., A. Rozenberg, T. Fabrin, C. Gonzalez-Cabrera, R. Parker, O. Beja, M. Prigge and P.
1035 Hegemann (2024). "Robust optogenetic inhibition with red-light-sensitive anion-conducting
1036 channelrhodopsins." Elife **12**: RP90100.

1037 Pereira, L., P. Kratsios, E. Serrano-Saiz, H. Sheftel, A. E. Mayo, D. H. Hall, J. G. White, B. LeBoeuf, L. R.
1038 Garcia, U. Alon and O. Hobert (2015). "A cellular and regulatory map of the cholinergic nervous system
1039 of *C. elegans*." Elife **4**: e12432.

1040 Piatkevich, K. D. and E. S. Boyden (2023). "Optogenetic control of neural activity: the Biophysics of
1041 microbial rhodopsins in neuroscience." Q Rev Biophys **57**(e1): 1-26.

1042 Priyam, A., B. J. Woodcroft, V. Rai, I. Moghul, A. Munagala, F. Ter, H. Chowdhary, I. Pieniak, L. J. Maynard,
1043 M. A. Gibbins, H. Moon, A. Davis-Richardson, M. Uludag, N. S. Watson-Haigh, R. Challis, H. Nakamura, E.
1044 Favreau, E. A. Gomez, T. Pluskal, G. Leonard, W. Rumpf and Y. Wurm (2019). "Sequenceserver: A modern
1045 graphical user interface for custom BLAST databases." Mol Biol Evol **36**(12): 2922-2924.

1046 Raizen, D. M. and L. Avery (1994). "Electrical activity and behavior in the pharynx of *Caenorhabditis*
1047 *elegans*." Neuron **12**(3): 483-495.

1048 Richter, D. J., C. Berney, J. F. H. Strassert, Y.-P. Poh, E. K. Herman, S. A. Muñoz-Gómez, J. G. Wideman, F.
1049 Burki and C. de Vargas (2022). "EukProt: A database of genome-scale predicted proteins across the
1050 diversity of eukaryotes." Peer Community Journal **2**: e56.

1051 Rozenberg, A. (2024). A catalog of natural channelrhodopsins (1.5) Zenodo.

1052 Rozenberg, A., J. Oppermann, J. Wietek, R. G. Fernandez Lahore, R. A. Sandaa, G. Bratbak, P. Hegemann
1053 and O. Béjà (2020). "Lateral gene transfer of anion-conducting channelrhodopsins between green algae
1054 and giant viruses." Curr. Biol. **30**: 4910-4920.

1055 Sakamoto, M. and T. Yokoyama (2025). "Probing neuronal activity with genetically encoded calcium and
1056 voltage fluorescent indicators." Neurosci Res **215**: 56-63.

1057 Schuler, C., E. Fischer, L. Shaltiel, W. Steuer Costa and A. Gottschalk (2015). "Arrhythmogenic effects of
1058 mutated L-type Ca^{2+}-channels on an optogenetically paced muscular pump in *Caenorhabditis elegans*."
1059 Sci Rep **5**: 14427.

1060 Shimono, K., M. Iwamoto, M. Sumi and N. Kamo (2000). "Effects of three characteristic amino acid
1061 residues of pharaonis phoborhodopsin on the absorption maximum." Photochem. Photobiol. **72**: 141-
1062 145.

1063 Shimono, K., M. Kitami, M. Iwamoto and N. Kamo (2000). "Involvement of two groups in reversal of the
1064 bathochromic shift of pharaonis phoborhodopsin by chloride at low pH." Biophys. Chem. **87**(2-3): 225-
1065 230.

1066 Sineshchekov, O. A., E. G. Govorunova, H. Li and J. L. Spudich (2015). "Gating mechanisms of a natural
1067 anion channelrhodopsin." Proc. Natl. Acad. Sci. USA **112**: 14236-14241.

1068 Sineshchekov, O. A., E. G. Govorunova, H. Li, Y. Wang and J. L. Spudich (2023). "Sequential absorption of
1069 two photons creates a bistable form of RubyACR responsible for its strong desensitization." Proc Natl
1070 Acad Sci U S A **120**(21): e2301521120.

1071 Sineshchekov, O. A., K.-H. Jung and J. L. Spudich (2002). "Two rhodopsins mediate phototaxis to low- and
1072 high-intensity light in *Chlamydomonas reinhardtii*." Proc. Natl. Acad. Sci. USA **99**: 8689-8694.

1073 Sineshchekov, O. A., H. Li, E. G. Govorunova and J. L. Spudich (2016). "Photochemical reaction cycle
1074 transitions during anion channelrhodopsin gating." Proc. Natl. Acad. Sci. USA **113**: E1993-2000.

Spudich, E. N., G. Ozorowski, E. V. Schow, D. J. Tobias, J. L. Spudich and H. Luecke (2012). "A transporter converted into a sensor, a phototaxis signaling mutant of bacteriorhodopsin at 3.0 A." J. Mol. Biol. **415**(3): 455-463.

Spudich, J. L. (2022). LogPro, Zenodo.

Sudo, Y., A. Okazaki, H. Ono, J. Yagasaki, S. Sugo, M. Kamiya, L. Reissig, K. Inoue, K. Ihara, H. Kandori, S. Takagi and S. Hayashi (2013). "A blue-shifted light-driven proton pump for neural silencing." J. Biol. Chem. **288**(28): 20624-20632.

Sunagawa, S., L. P. Coelho, S. Chaffron, J. R. Kultima, K. Labadie, G. Salazar, B. Djahanschiri, G. Zeller, D. R. Mende, A. Alberti, F. M. Cornejo-Castillo, P. I. Costea, C. Cruaud, F. d'Ovidio, S. Engelen, I. Ferrera, J. M. Gasol, L. Guidi, F. Hildebrand, F. Kokoszka, C. Lepoivre, G. Lima-Mendez, J. Poulain, B. T. Poulos, M. Royo-Llonch, H. Sarmento, S. Vieira-Silva, C. Dimier, M. Picheral, S. Searson, S. Kandels-Lewis, c. Tara Oceans, C. Bowler, C. de Vargas, G. Gorsky, N. Grimsley, P. Hingamp, D. Iudicone, O. Jaillon, F. Not, H. Ogata, S. Pesant, S. Speich, L. Stemmann, M. B. Sullivan, J. Weissenbach, P. Wincker, E. Karsenti, J. Raes, S. G. Acinas and P. Bork (2015). "Ocean plankton. Structure and function of the global ocean microbiome." Science **348**(6237): 1261359.

Tajima, S., Y. S. Kim, M. Fukuda, Y. Jo, P. Y. Wang, J. M. Paggi, M. Inoue, E. F. X. Byrne, K. E. Kishi, S. Nakamura, C. Ramakrishnan, S. Takaramoto, T. Nagata, M. Konno, M. Sugiura, K. Katayama, T. E. Matsui, K. Yamashita, S. Kim, H. Ikeda, J. Kim, H. Kandori, R. O. Dror, K. Inoue, K. Deisseroth and H. E. Kato (2023). "Structural basis for ion selectivity in potassium-selective channelrhodopsins." Cell **186**(20): 4325-4344.

Tashiro, R., K. Sushmita, S. Hososhima, S. Sharma, S. Kateriya, H. Kandori and S. P. Tsunoda (2021). "Specific residues in the cytoplasmic domain modulate photocurrent kinetics of channelrhodopsin from the alga *Klebsormidium nitens*." Commun. Biol. **4**: 235.

Tikhonenkov, D. V., K. V. Mikhailov, R. M. R. Gawryluk, A. O. Belyaev, V. Mathur, S. A. Karpov, D. G. Zagumyonnyi, A. S. Borodina, K. I. Prokina, A. P. Mylnikov, V. V. Aleoshin and P. J. Keeling (2022). "Microbial predators form a new supergroup of eukaryotes." Nature **612**(7941): 714-719.

Torruella, G., A. de Mendoza, X. Grau-Bove, M. Anto, M. A. Chaplin, J. del Campo, L. Eme, G. Perez-Cordon, C. M. Whipps, K. M. Nichols, R. Paley, A. J. Roger, A. Sitja-Bobadilla, S. Donachie and I. Ruiz-Trillo (2015). "Phylogenomics reveals convergent evolution of lifestyles in close relatives of animals and fungi." Curr Biol **25**(18): 2404-2410.

Trojanowski, N. F., O. Padovan-Merhar, D. M. Raizen and C. Fang-Yen (2014). "Neural and genetic degeneracy underlies *Caenorhabditis elegans* feeding behavior." J Neurophysiol **112**(4): 951-961.

Trojanowski, N. F., D. M. Raizen and C. Fang-Yen (2016). "Pharyngeal pumping in *Caenorhabditis elegans* depends on tonic and phasic signaling from the nervous system." Sci Rep **6**: 22940.

Tsujimura, M., T. Noji, K. Saito, K. Kojima, Y. Sudo and H. Ishikita (2021). "Mechanism of absorption wavelength shifts in anion channelrhodopsin-1 mutants." Biochim. Biophys. Acta Bioenerg. **1862**: 148349.

Tucker, K., S. Sridharan, H. Adesnik and S. G. Brohawn (2022). "Cryo-EM structures of the channelrhodopsin ChRmine in lipid nanodiscs." Nat Commun **13**(1): 4842.

Váró, G., L. S. Brown, R. Needleman and J. K. Lanyi (1996). "Proton transport by halorhodopsin." Biochemistry **35**(21): 6604-6611.

Villar, E., T. Vannier, C. Vernette, M. Lescot, M. Cuenca, A. Alexandre, P. Bachelerie, T. Rosnet, E. Pelletier, S. Sunagawa and P. Hingamp (2018). "The Ocean Gene Atlas: exploring the biogeography of plankton genes online." Nucleic Acids Res. **46**(W1): W289-W295.

Volkov, O., K. Kovalev, V. Polovinkin, V. Borshchevskiy, C. Bamann, R. Astashkin, E. Marin, A. Popov, T. Balandin, D. Willbold, G. Buldt, E. Bamberg and V. Gordeliy (2017). "Structural insights into ion conduction by channelrhodopsin 2." Science **358**(6366): eaan8862.

Wang, Y. Z., K. Natsume, T. Tanaka, S. Hososhima, R. Tashiro, F. K. Sano, H. Akasaka, S. P. Tsunoda, W. Shihoya, H. Kandori and O. Nureki (2025). "Cryo-EM structure of a blue-shifted channelrhodopsin from *Klebsormidium nitens*." Nat Commun **16**(1): 5297.

Xue, M., B. V. Atallah and M. Scanziani (2014). "Equalizing excitation-inhibition ratios across visual cortical neurons." Nature **511**(7511): 596-600.

Zabelskii, D., A. Alekseev, K. Kovalev, V. Rankovic, T. Balandin, D. Soloviov, D. Bratanov, E. Savelyeva, E. Podolyak, D. Volkov, S. Vaganova, R. Astashkin, I. Chizhov, N. Yutin, M. Rulev, A. Popov, A. S. Eria-Oliveira, T. Rokitskaya, T. Mager, Y. Antonenko, R. Rosselli, G. Armeev, K. Shaitan, M. Vivaudou, G. Buldt, A. Rogachev, F. Rodriguez-Valera, M. Kirpichnikov, T. Moser, A. Offenhausser, D. Willbold, E. Koonin, E. Bamberg and V. Gordeliy (2020). "Viral rhodopsins 1 are an unique family of light-gated cation channels." Nat. Commun. **11**(1): 5707.

1134 **Figure 1**

1135

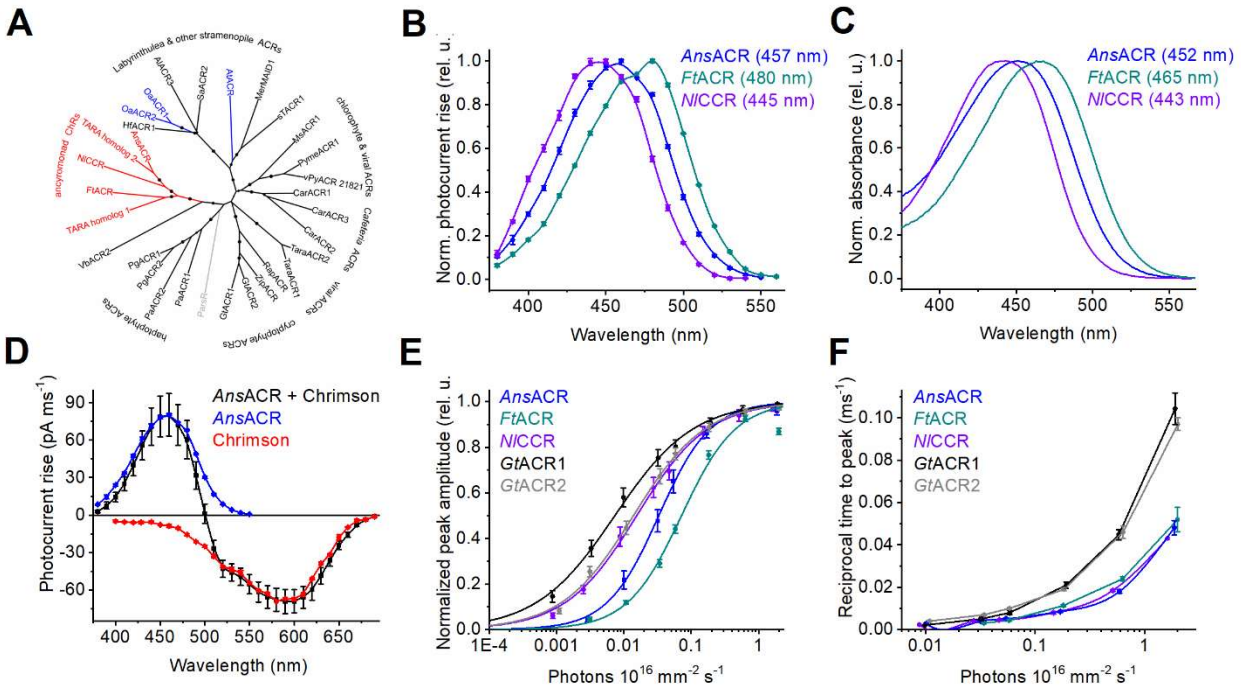

1136

Figure 1 - figure supplement 1

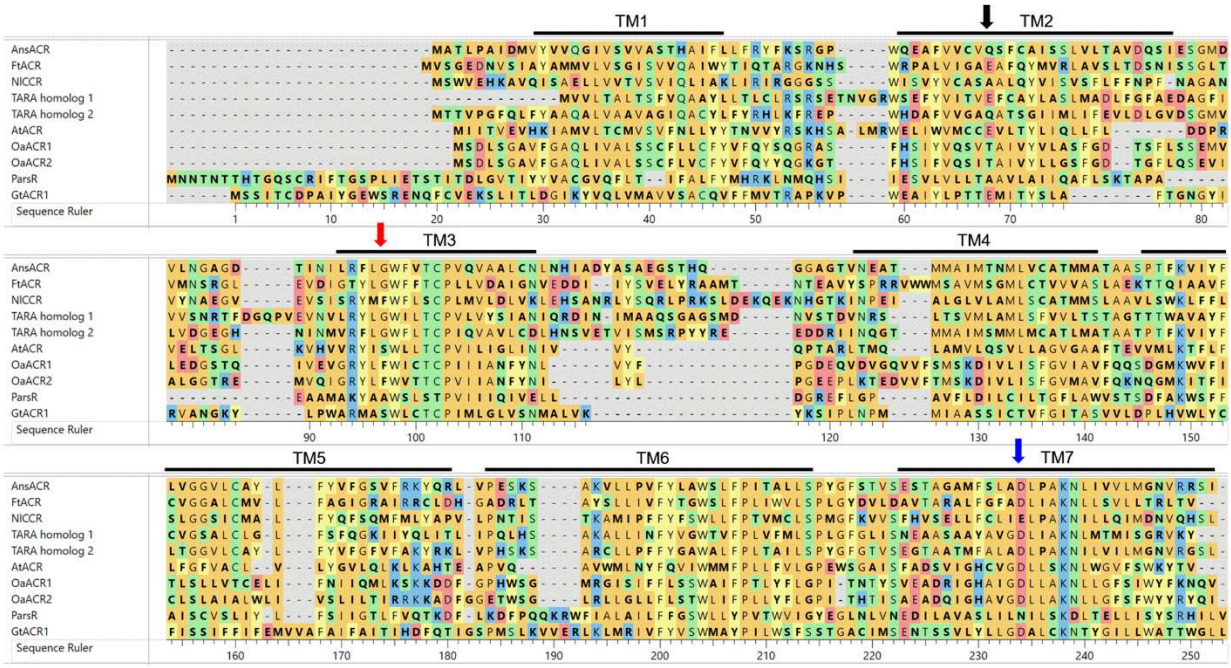

1140 **Figure 1 - figure supplement 2**

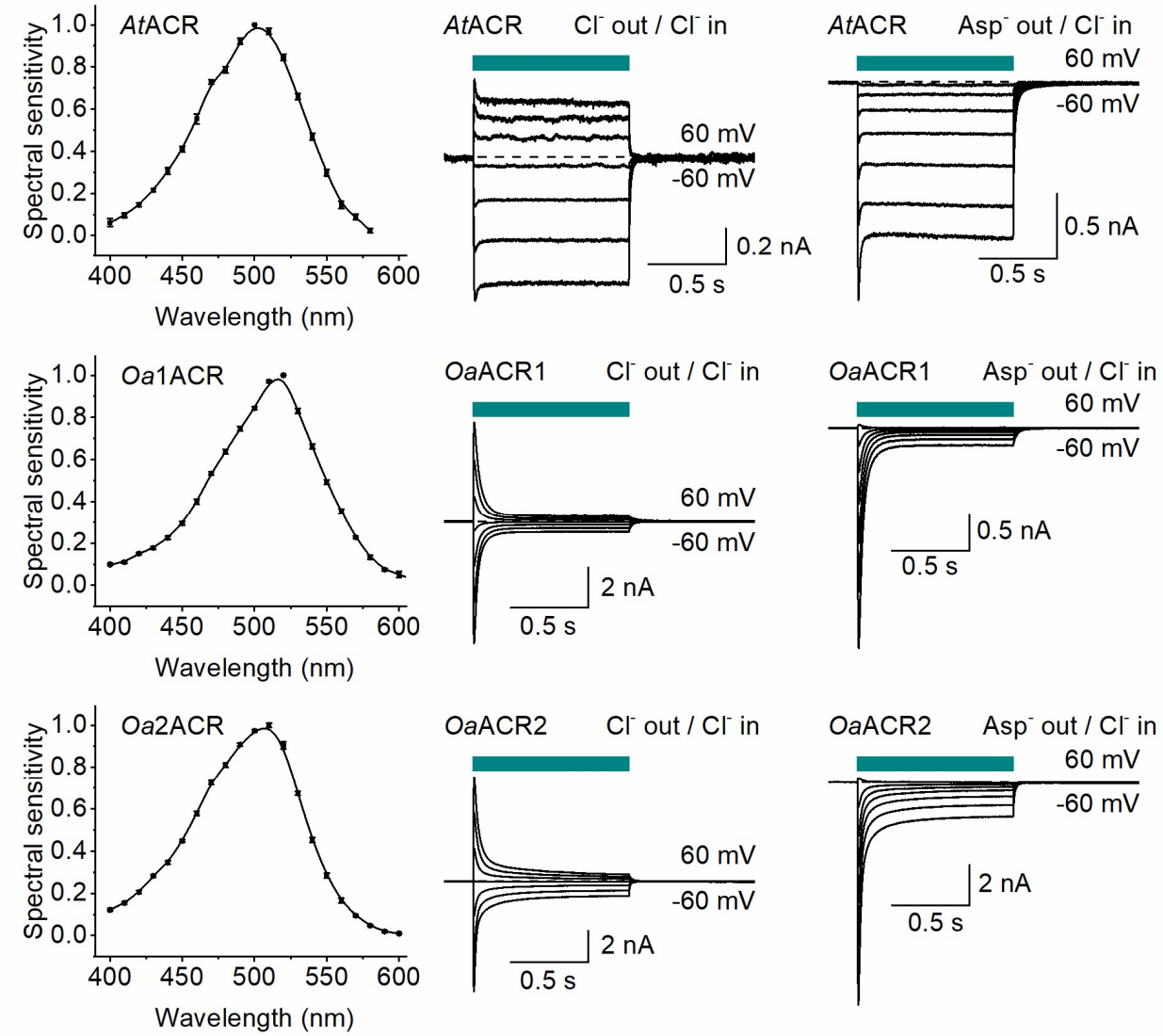

1141

1142

1143 **Figure 1 - figure supplement 3**

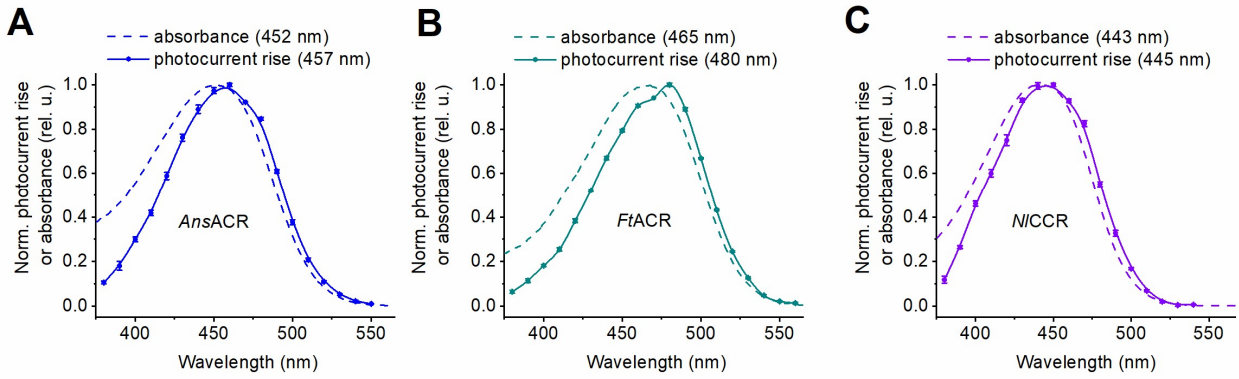

1144

1145

1146

1147 **Figure 1 - figure supplement 4**

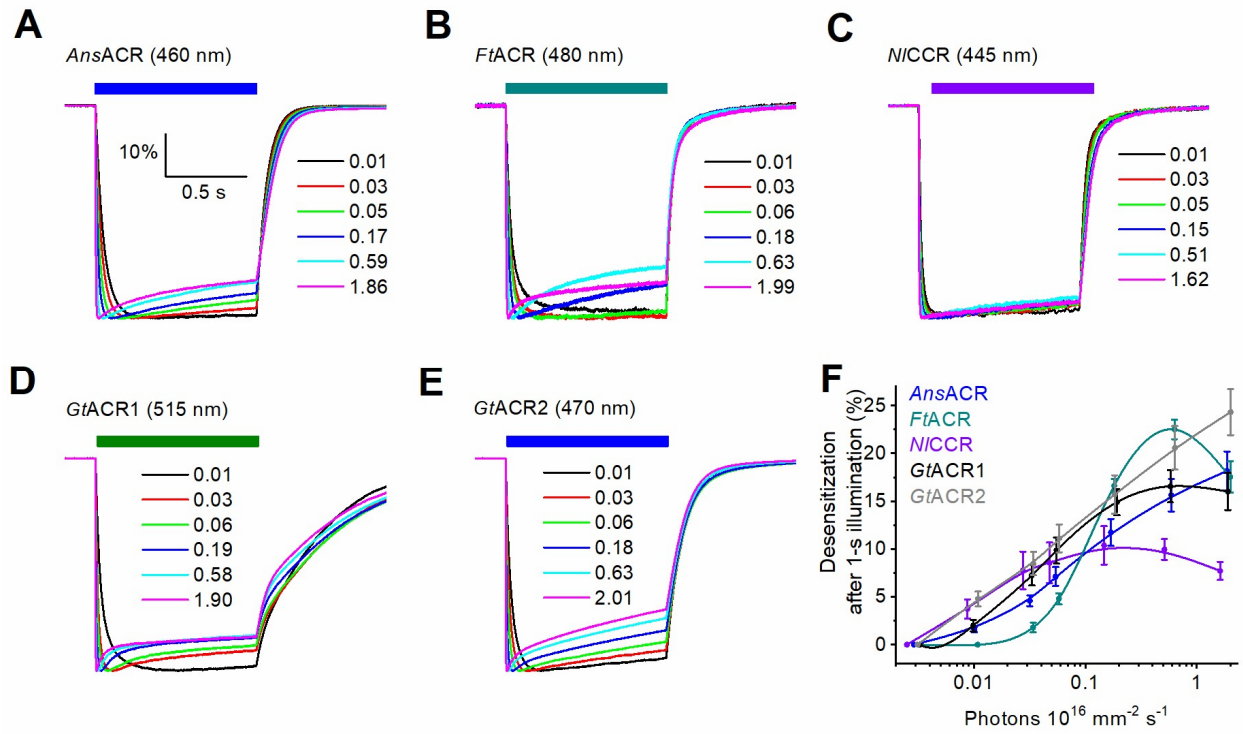

1148

1149

1150 **Figure 1 - figure supplement 5**

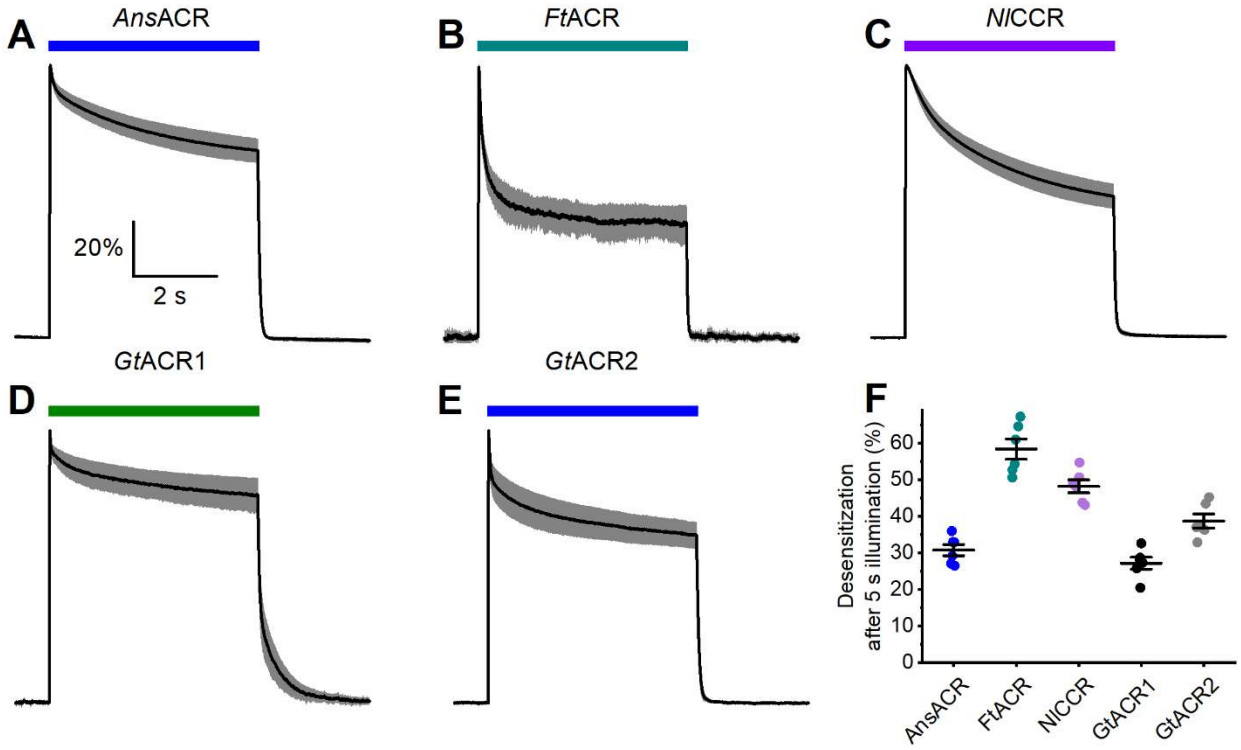

1151

1152

1153 **Figure 2**

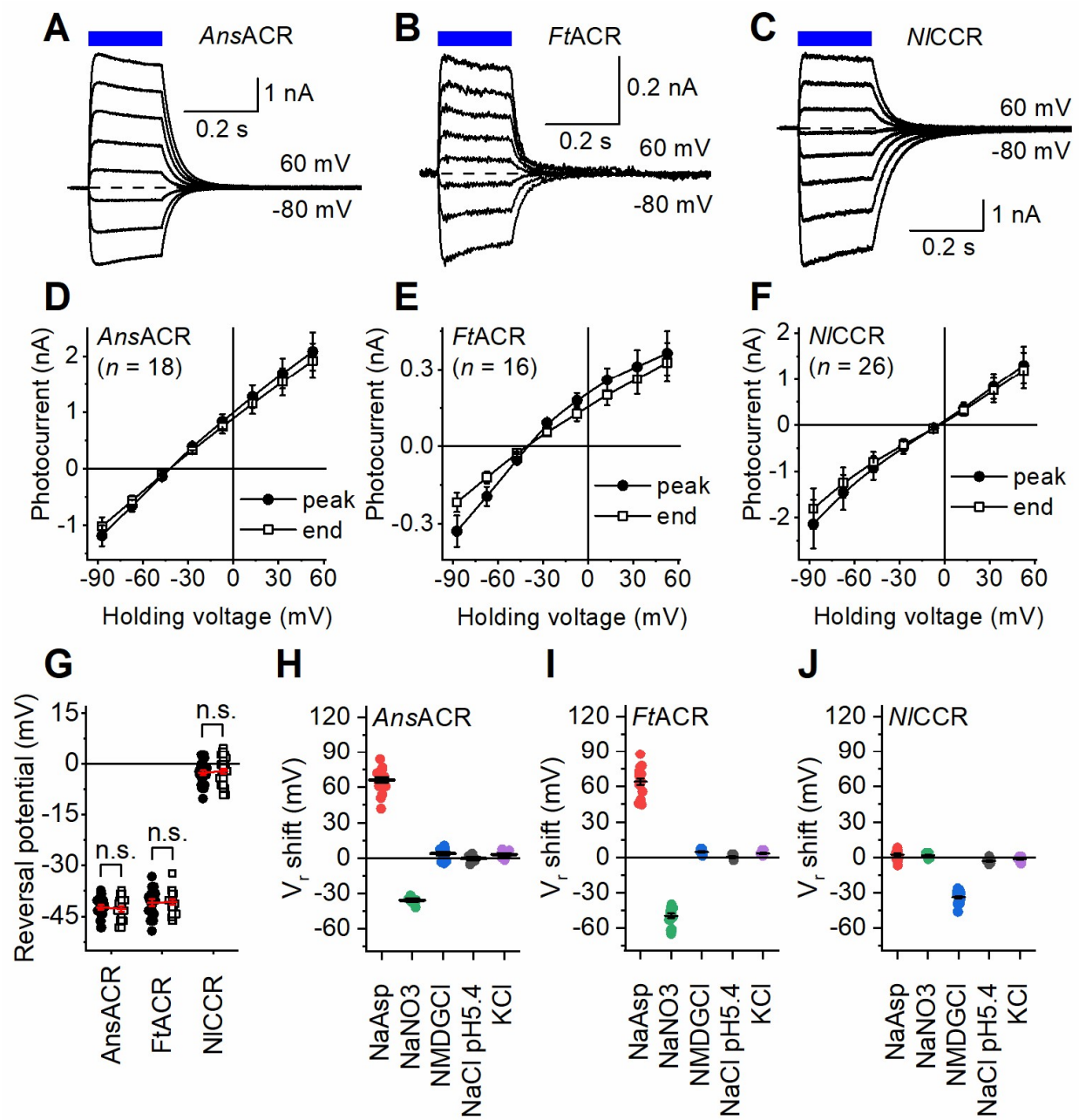

1154

1155

1156 **Figure 2 - figure supplement 1**

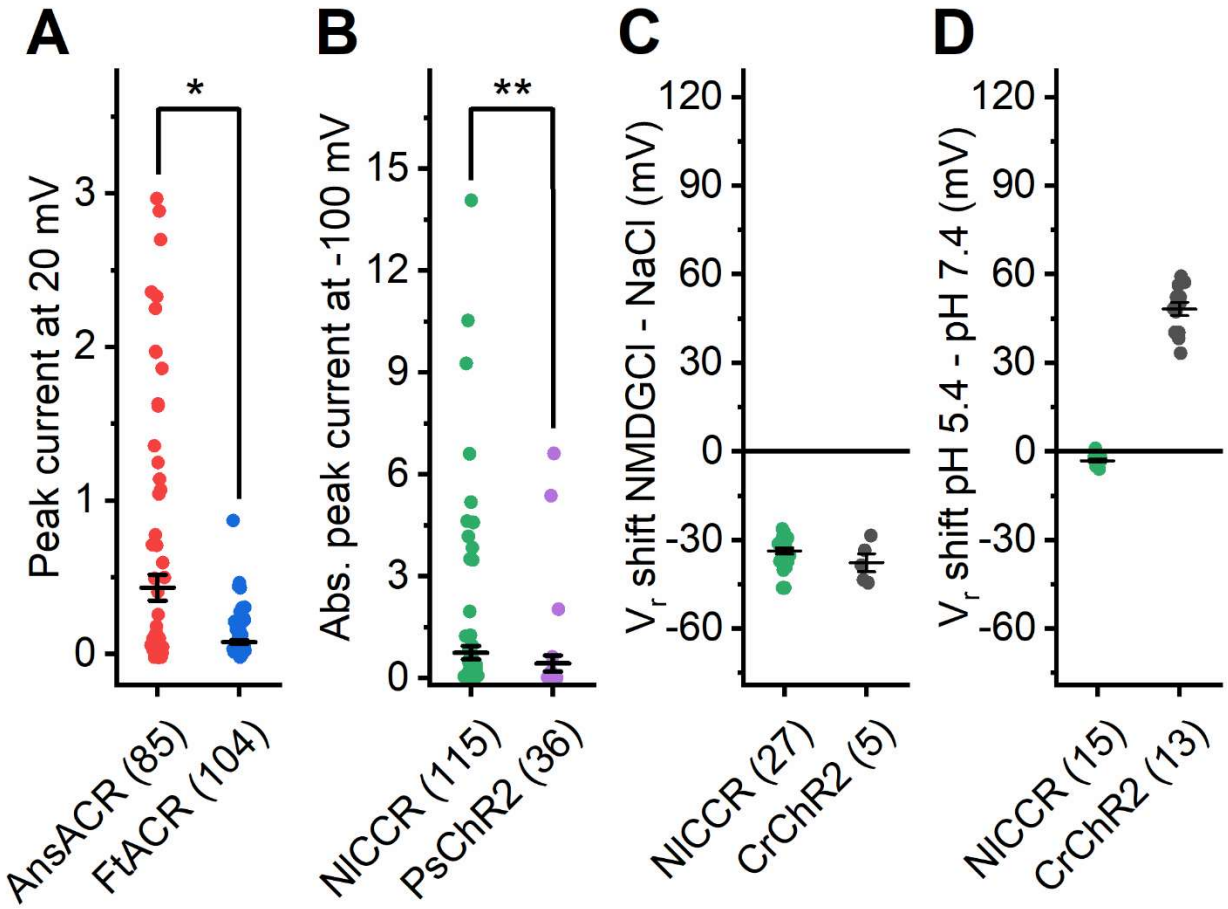

1157

1158

1159 **Figure 2 - figure supplement 2**

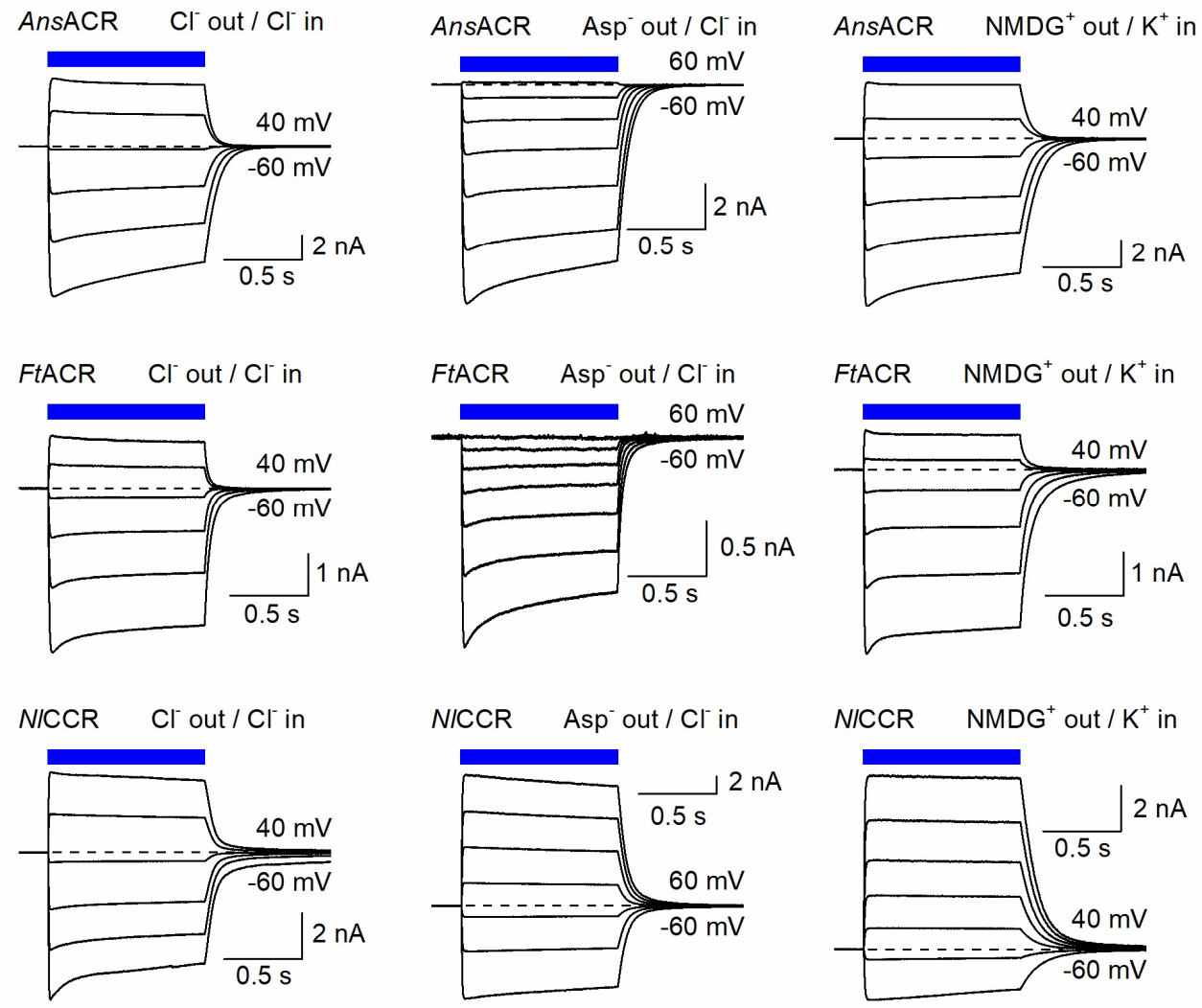

1160

1161

1162 **Figure 3**

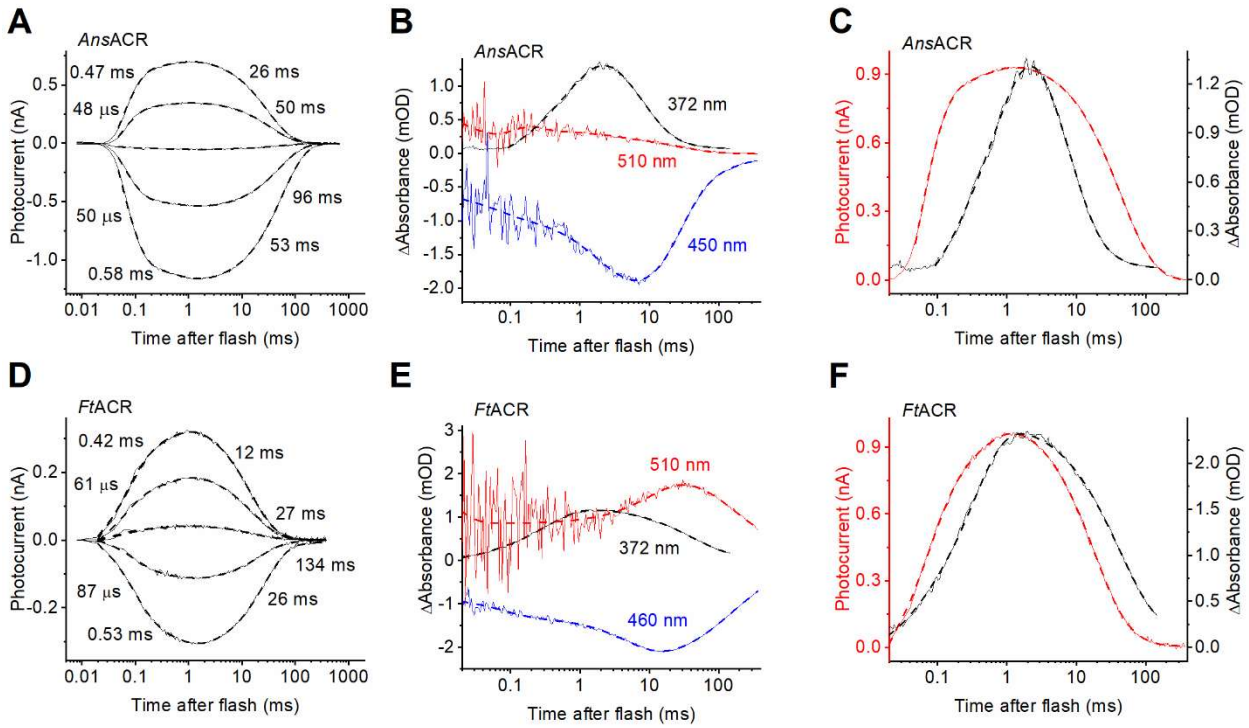

1163

1164

1165 **Figure 3 - figure supplement 1**

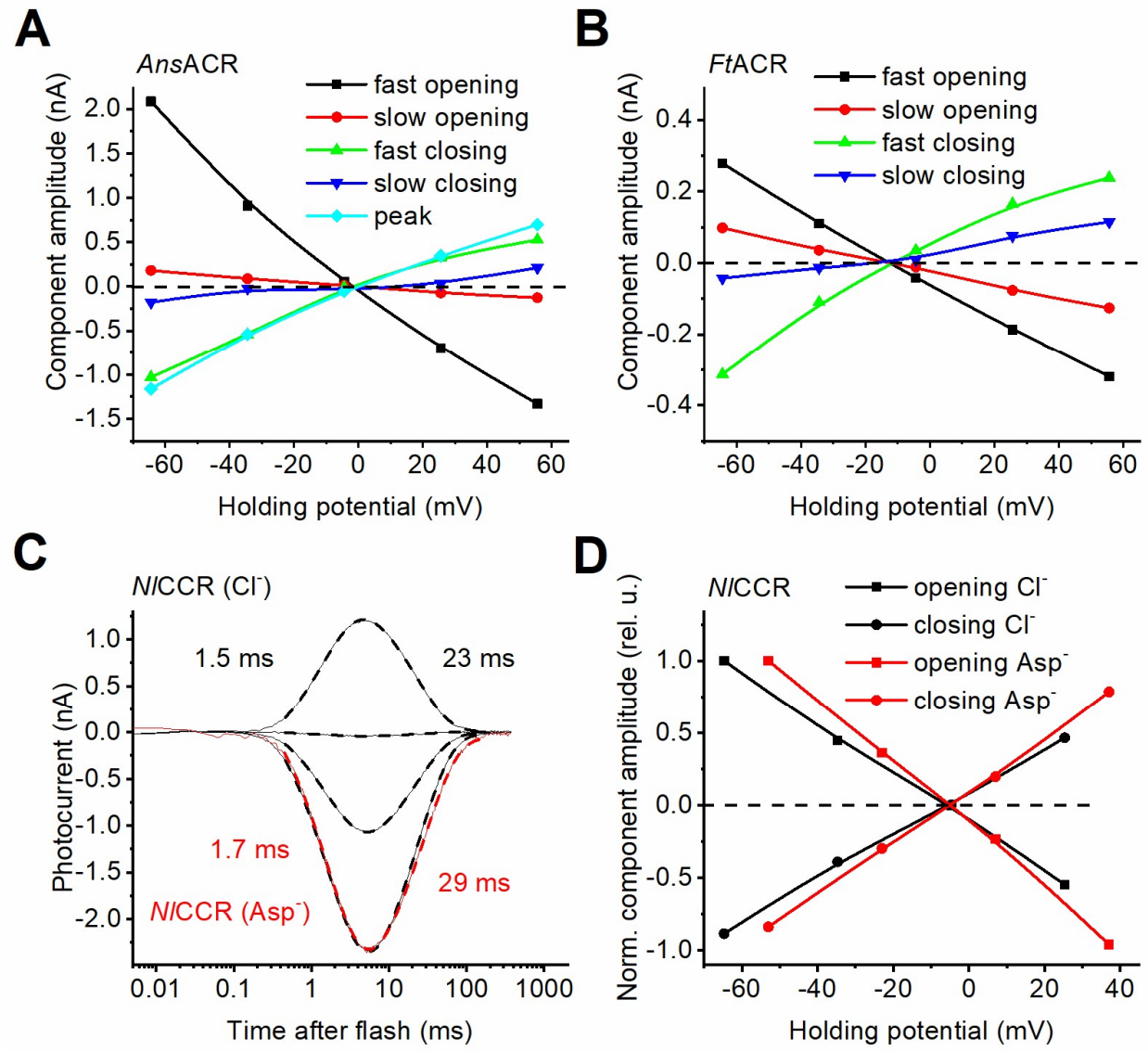

1166

1167

1168 **Figure 4**

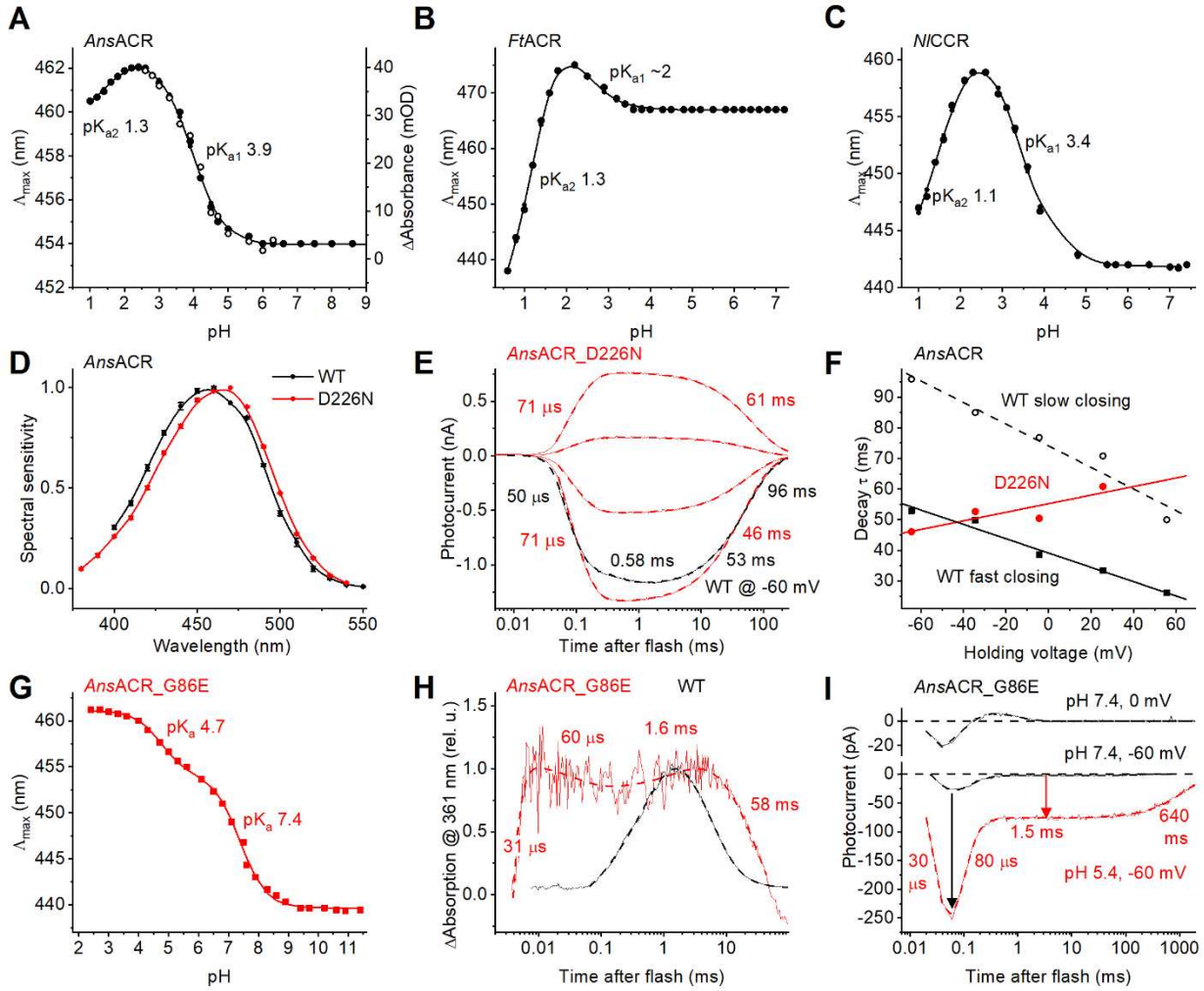

1169

1170

1171 **Figure 4 - figure supplement 1**

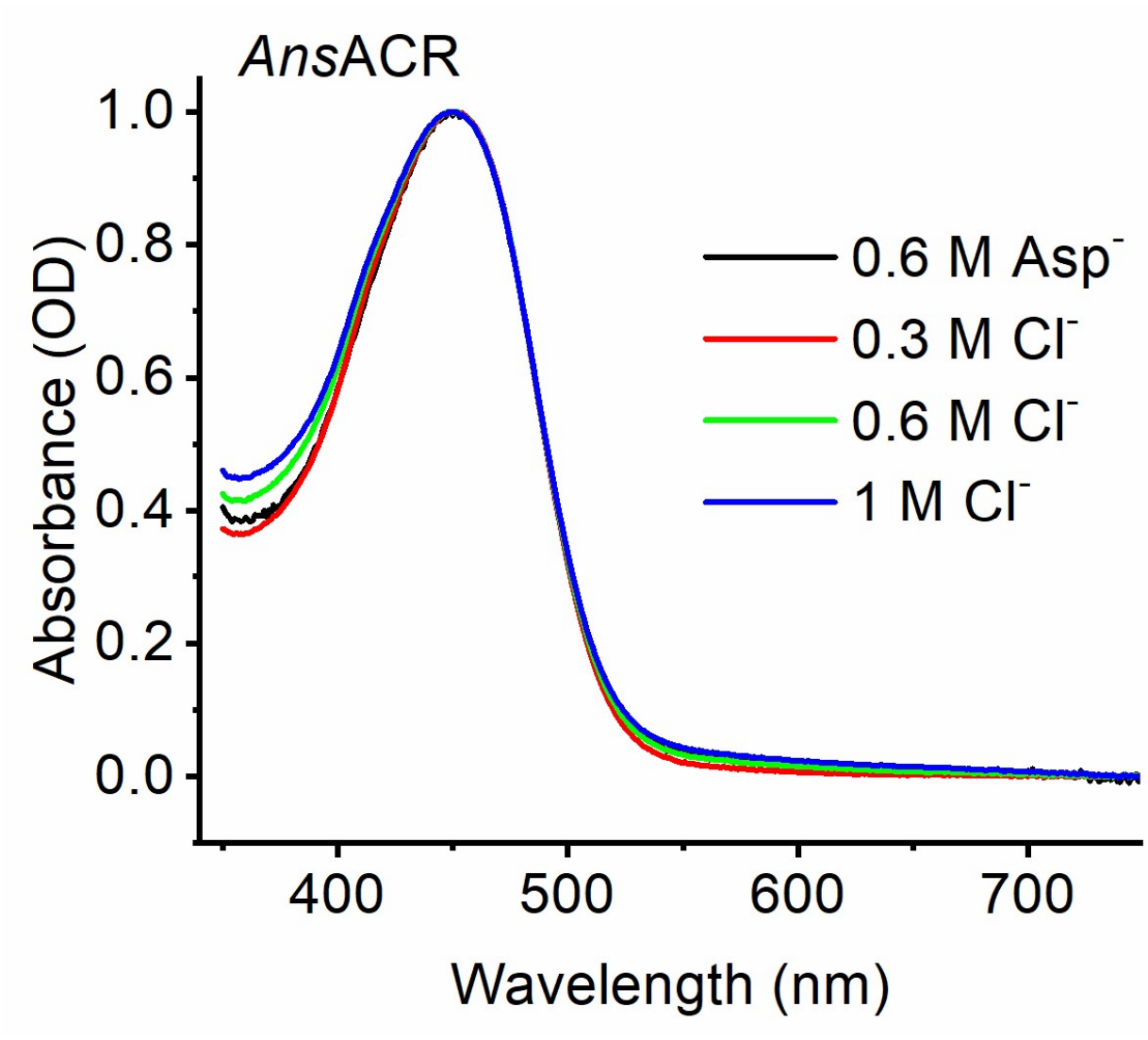

1172

1173

1174 **Figure 4 - figure supplement 2**

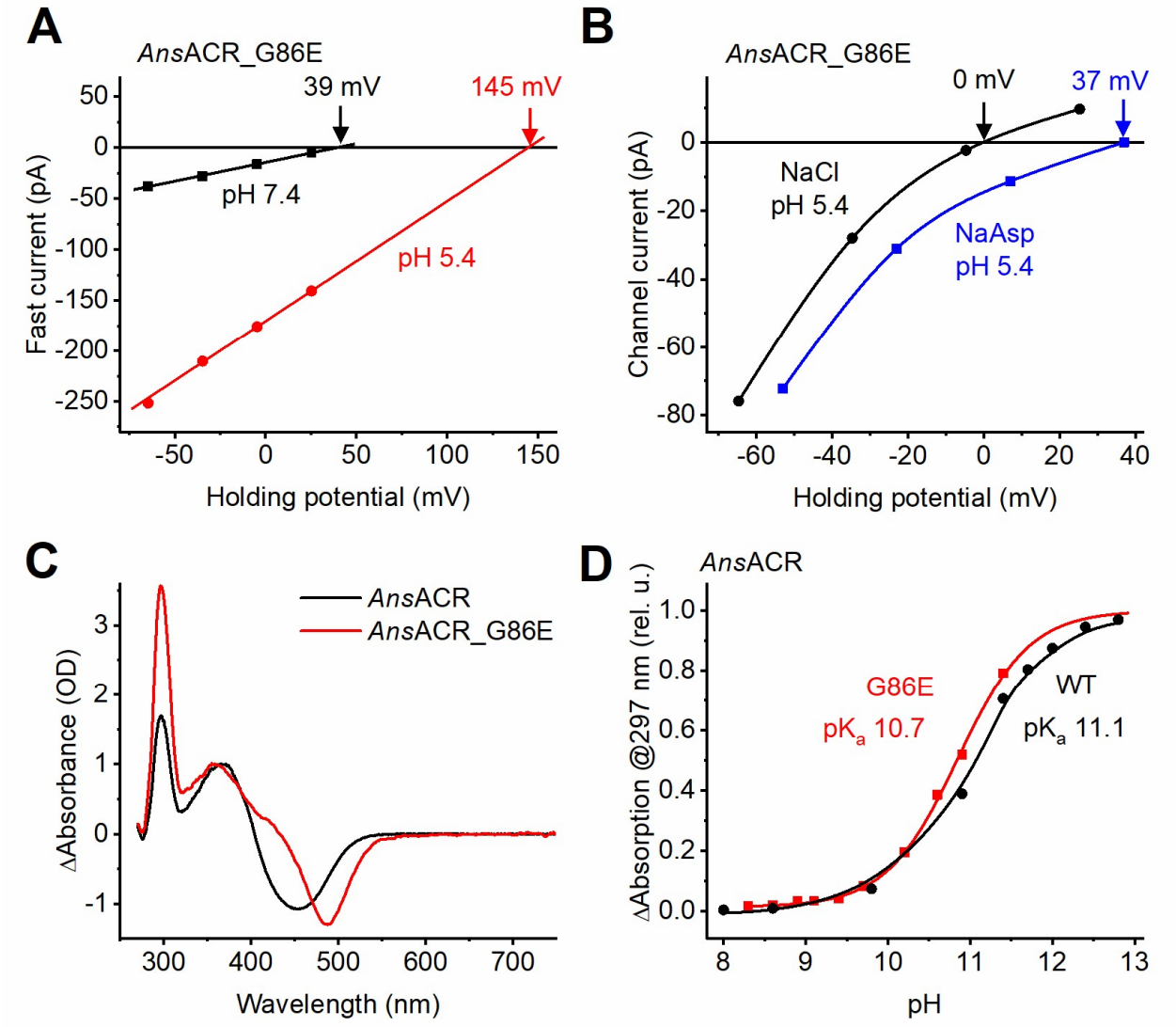

1175

1176

1177 **Figure 4 - figure supplement 3**

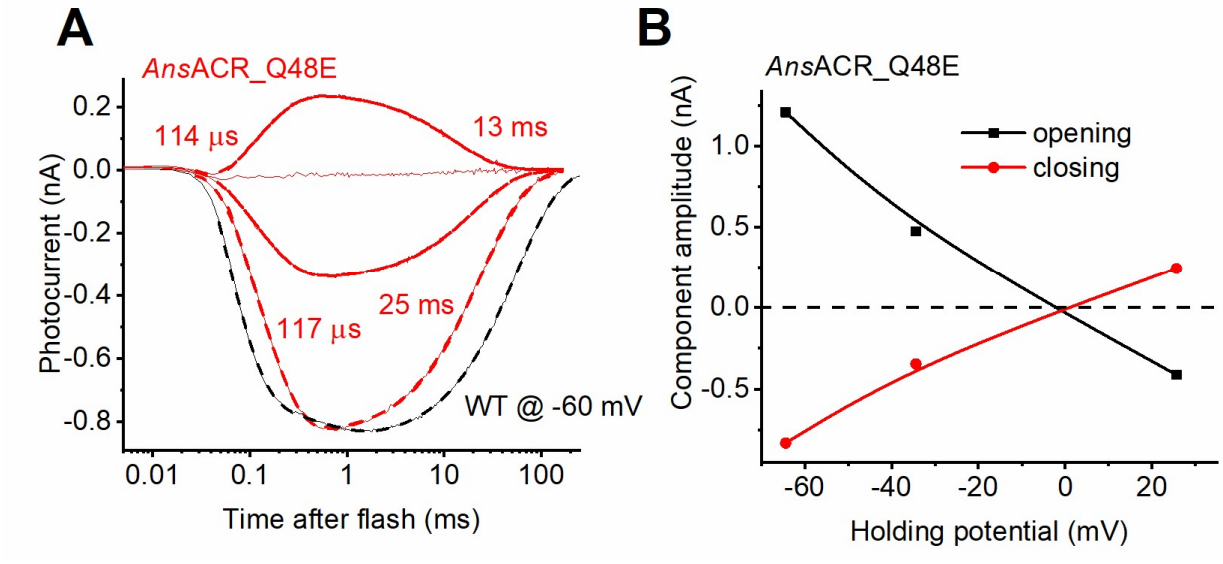

1178

1179

1180 **Figure 5**

A

*Ans*ACR	G86	**M134**	**A229**	**A138**	**Q94**	T90	D226	**P228**
*Ft*ACR	G88	**M140**	**A235**	V144	L96	T92	D232	I234
*Nl*CCR	**F85**	**M141**	**A236**	**A145**	M93	**S89**	**E233**	**P235**
*Hf*ACR1	**F104**	**M143**	**A242**	G147	I112	T108	D239	F241
Chrimson	E165	**M201**	**A298**	G205	I173	**S169**	D295	I297
BR	D85	**M118**	**A215**	G122	L93	T89	D212	S214
*Gt*ACR1	S97	C133	C237	G137	M105	T101	D234	L236
*Ps*ChR2	E106	**G142**	S239	**A146**	I114	T110	D236	L238
*Kn*ChR	E121	**A157**	S253	**A161**	I129	T125	D250	L252

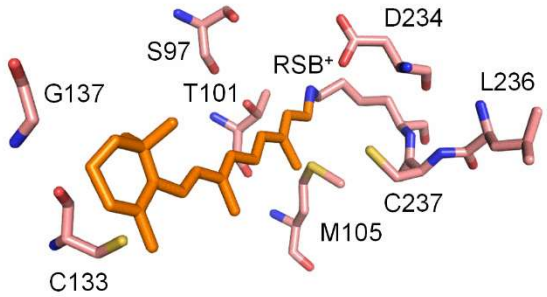

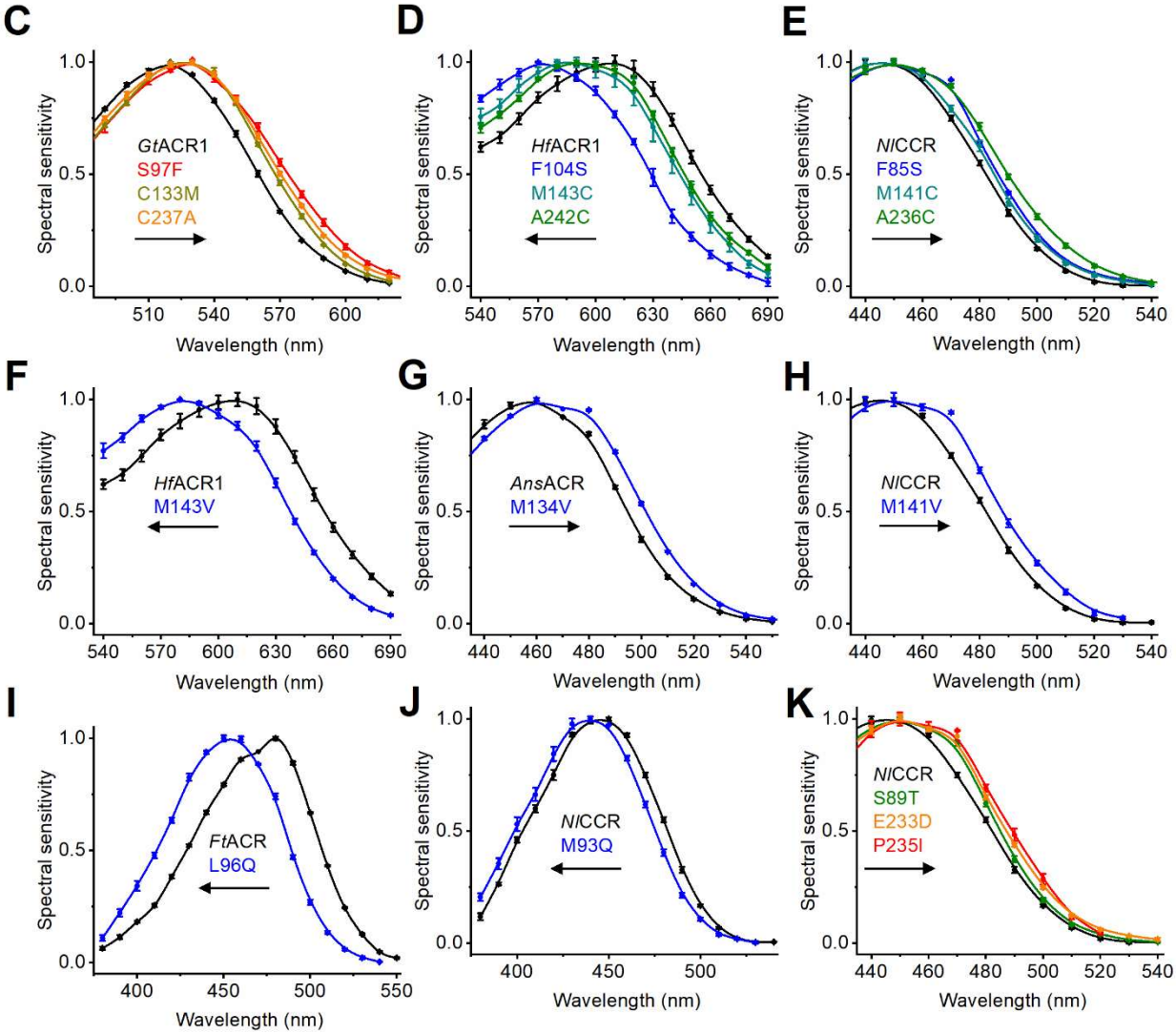

1181

1182

1183 **Figure 5 - figure supplement 1**

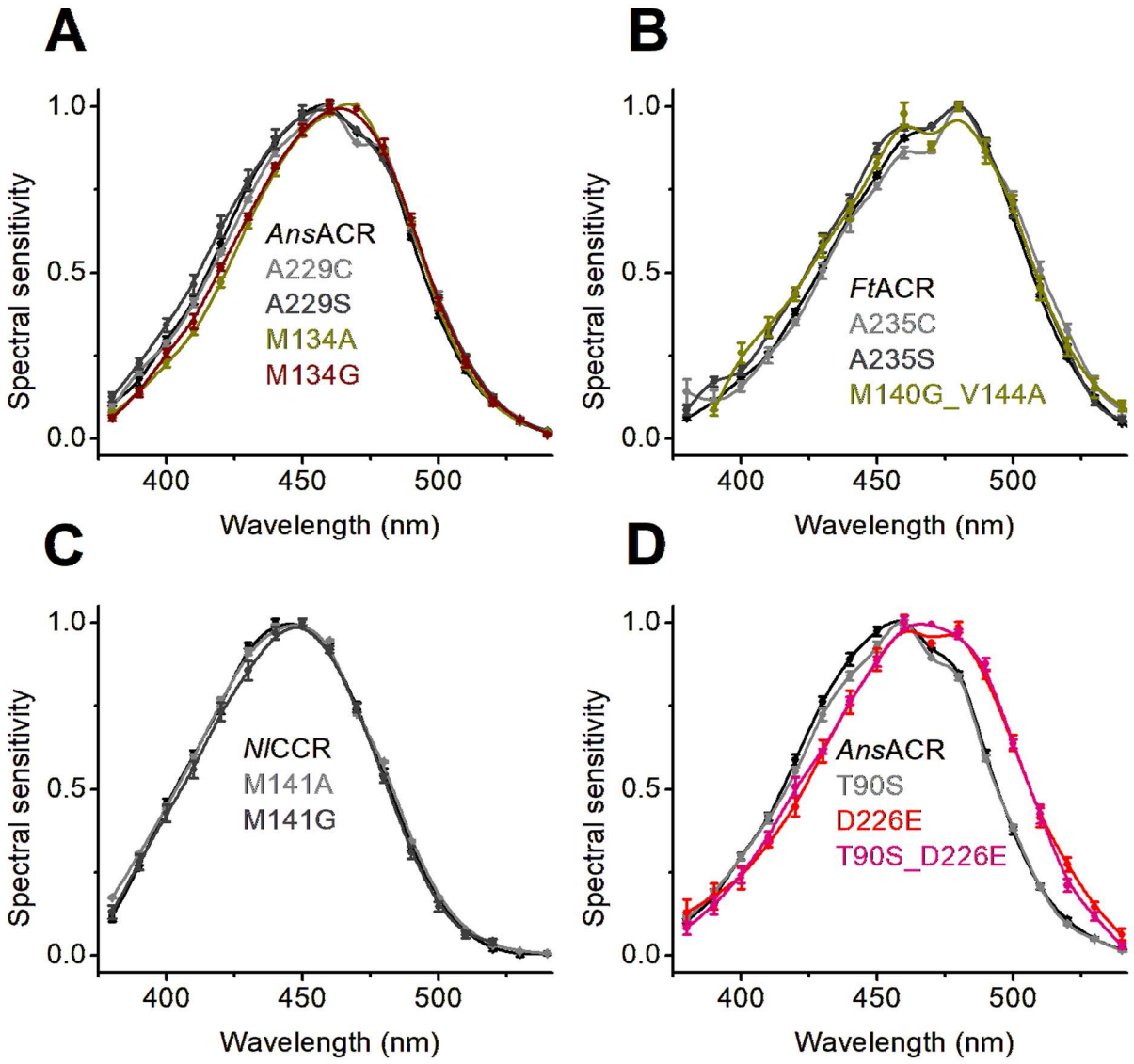

1184

1185

1186 **Figure 6**

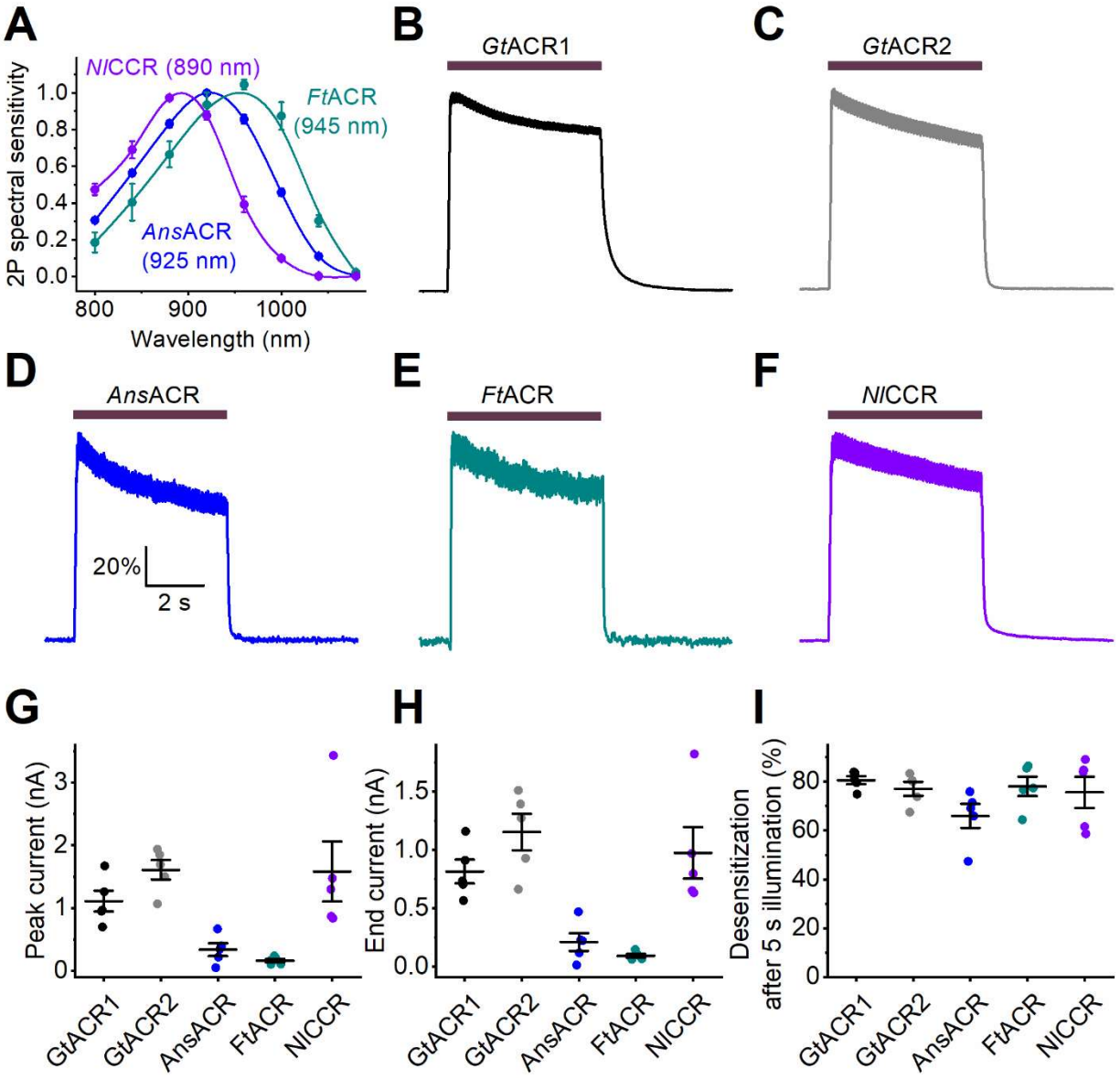

1187

1188

1189 **Figure 6 - figure supplement 1**

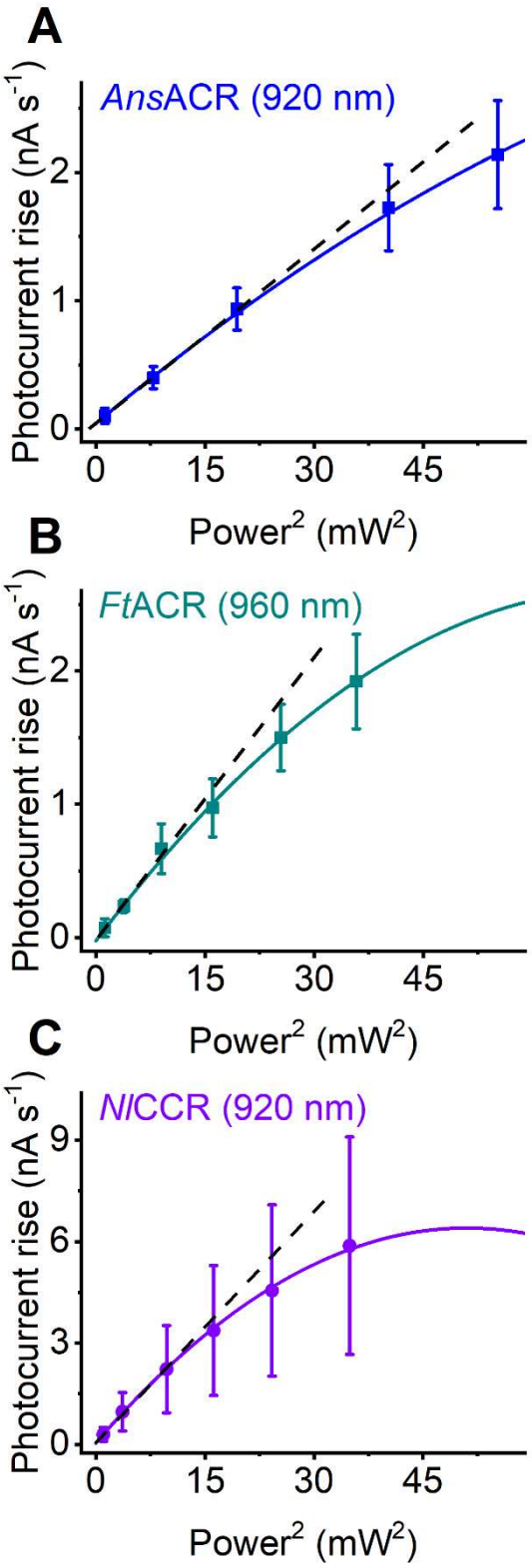

1190

1191 **Figure 7**

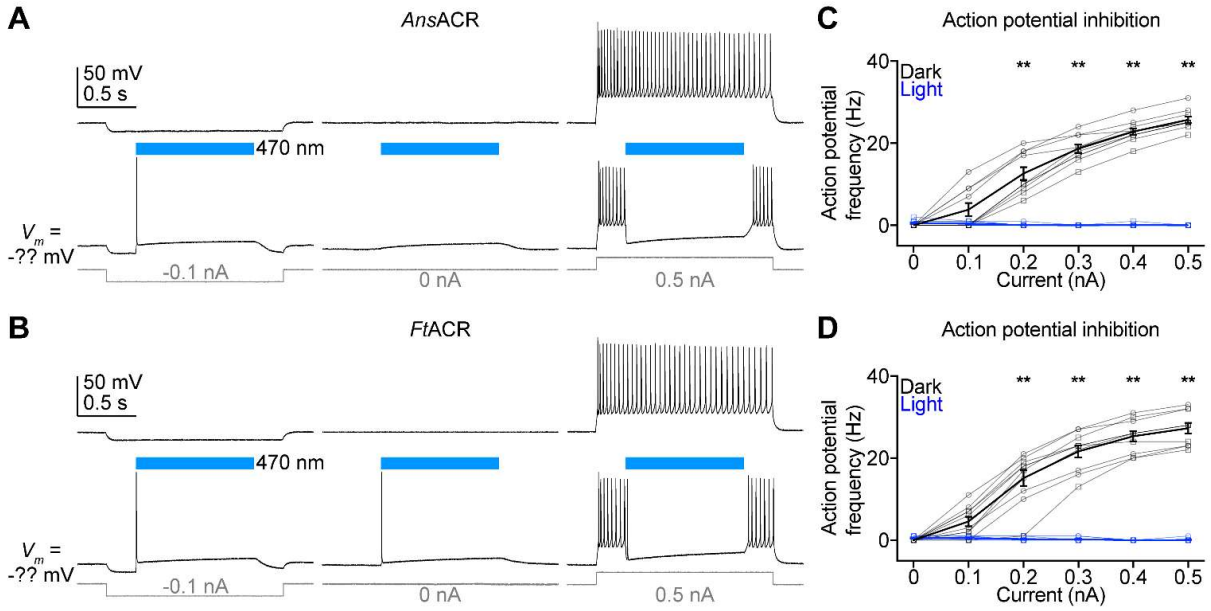

1192

1193

1194 **Figure 7 - figure supplement 1**

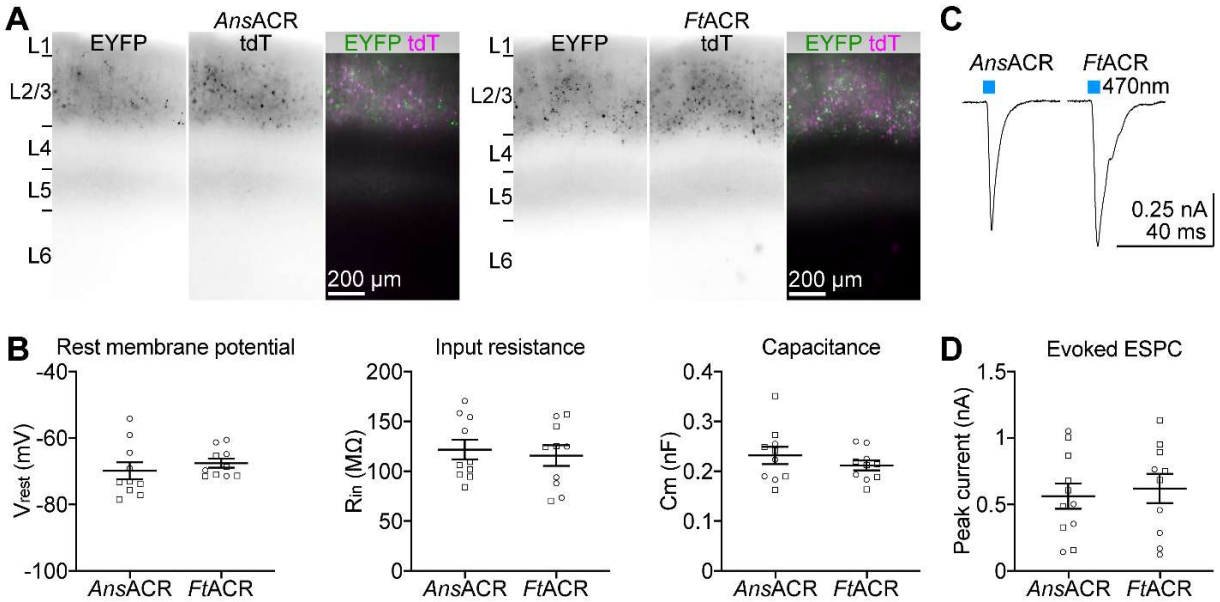

1195

1196

1197 **Figure 8**

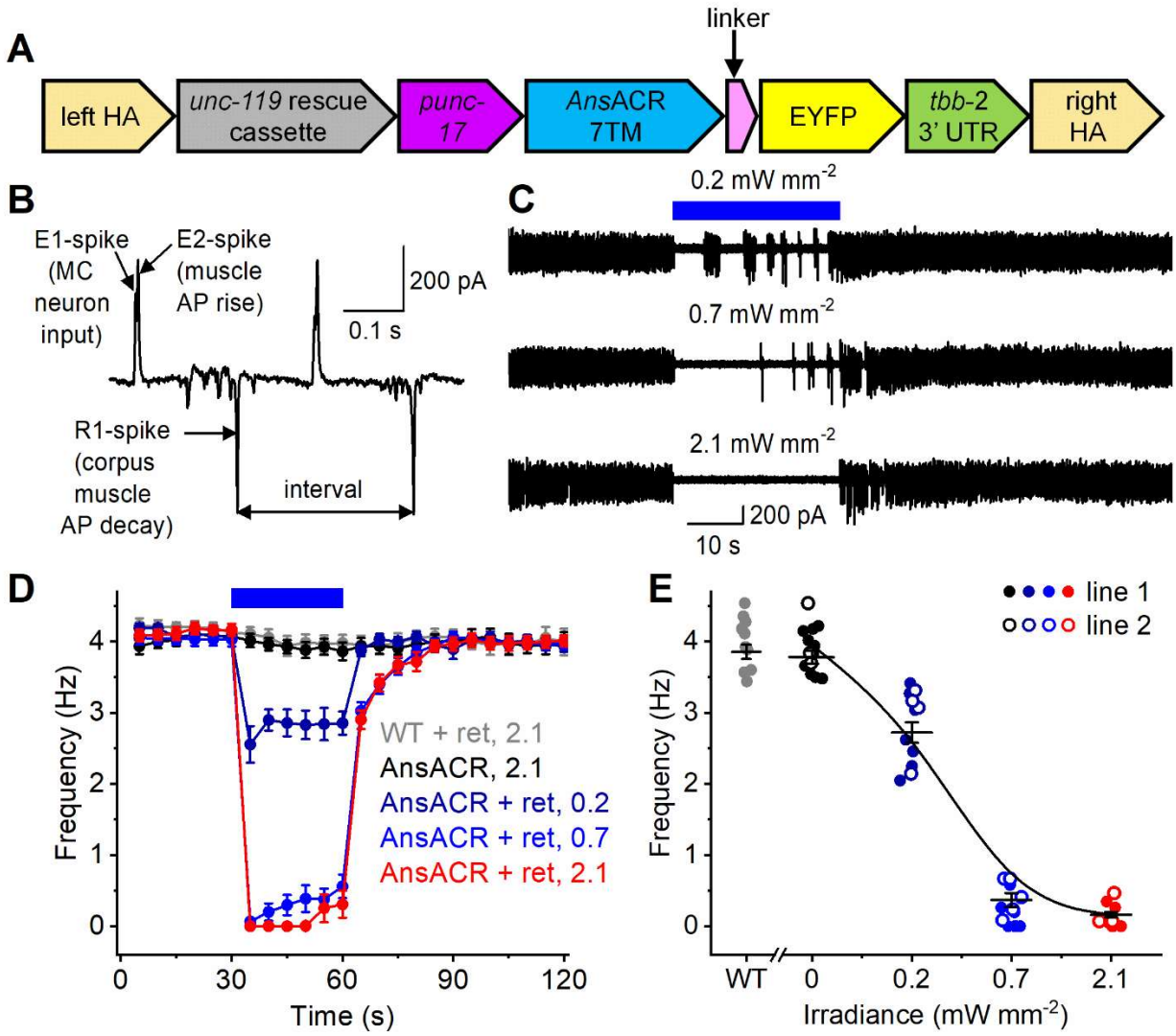

1198

1199